Comprehensive anisotropic linear optical properties of the Weyl semimetals TaAs and NbAs

Rui Zu [1] Mingqiang Gu,[2,*] Lujin Min [1] Chaowei Hu,[3] Ni Ni,[3] Zhiqiang Mao,[4]
James M. Rondinelli [5] and Venkatraman Gopalan [1,4,6,†]

[1]*Department of Materials Science and Engineering, Pennsylvania State University, University Park, Pennsylvania 16802, USA*
[2]*Shenzhen Institute for Quantum Science and Engineering (SIQSE) and Department of Physics,*
Southern University of Science and Technology, Shenzhen 518055, China
[3]*Department of Physics and Astronomy and California NanoSystems Institute, University of California, Los Angeles, California 90095, USA*
[4]*Department of Physics, Pennsylvania State University, University Park, Pennsylvania 16802, USA*
[5]*Department of Materials Science and Engineering, Northwestern University, Evanston, Illinois 60208, USA*
[6]*Department of Engineering Science and Mechanics, Pennsylvania State University, University Park, Pennsylvania 16802, USA*

TaAs and NbAs are two of the earliest identified Weyl semimetals that possess many intriguing optical properties, such as chirality-dependent optical excitations and giant second harmonic generation (SHG). Linear and nonlinear optics have been employed as tools to probe the Weyl physics in these crystals. Here, we extend these studies to address two important aspects: determining the complete anisotropic dielectric response and exploring if and how they can reveal essential Weyl physics. We determine the complete anisotropic dielectric functions of TaAs and NbAs by combining spectroscopic ellipsometry and density functional theory (DFT). Parameterized Lorentz oscillators are reported from 1.2–6 eV (experiment) and 0–6 eV (DFT), and good agreement is shown between them. Both linear and nonlinear optical properties have been previously reported to reveal Weyl physics. We suggest that strong optical resonances from trivial bands are the likely origin of the large optical SHG previously reported at these energies. Furthermore, by comparing the contribution of a small k-space centered around the Weyl cones with the total linear dielectric function, we find that these contributions are highly anisotropic and are $<25\%$ of the total dielectric function below 0.5 eV; above 1 eV, these contributions are negligible. Thus, the study of Weyl physics using optical techniques requires very low energies, and even there, a careful assessment is required in distinguishing the much smaller contributions of the Weyl bands from the dominant contributions of the trivial bands and Drude response to the total dielectric function.

I. INTRODUCTION

Although Weyl fermions were initially predicted in high-energy physics [1], it was first experimentally discovered in condensed matter, namely, the TaAs family [2]. Weyl fermions can be described as low-energy excitations near the Weyl nodes which represent the crossing points of singly degenerate bands in the presence of broken inversion symmetry or broken time-reversal symmetry. Weyl nodes appear in pairs with opposite chiralities; the bulk and surface state correspondence results in surface Fermi arcs. All these hallmarks of Weyl states have been demonstrated experimentally [3–10]. Weyl fermions give rise to a wide range of exotic transport properties [11], such as extremely high mobility [12], negative longitudinal magnetoresistance caused by chiral anomaly [13], and intrinsic anomalous Hall effect [14–17].

Optical measurements have been used as powerful techniques to characterize the exotic properties of Weyl semimetal states [18–22]. To explore the linear band crossing near the Fermi level, the temperature-dependent Drude behavior in the low-energy range and linear optical conductivity near the Weyl points have been explored [22–24]. The optical transitions in TaAs near the two types of Weyl nodes (labeled W1 and W2) have been identified to be <0.1 eV (for W1) and <0.2 eV (for W2) [23]. Due to the intrinsic noncentrosymmetry in the TaAs family, strongly anisotropic second harmonic generation (SHG) and circular photogalvanic effect have been observed, prompting further interest in higher-order nonlinear and coupled optical properties [18,25]. The giant SHG response in the TaAs family has been attributed to linear resonances as well as the shift current [25–28]. While extensive studies have focused on exploring the spectroscopic behavior at energies near Weyl points [21–23] and the optical resonances that contribute to giant SHG [26], the complete anisotropic linear optical susceptibility tensor, anisotropic complex refractive indices, and the band- and momentum-resolved optical transitions in TaAs and NbAs across the visible and near-infrared spectrum remain unreported. To that end, we report the complete anisotropic linear optical properties of both TaAs and NbAs and discuss the consequences of anisotropy in utilizing optical probes for probing Weyl physics.

Previous studies on the natural (112) planes of the crystal were focused on optical SHG, terahertz emission, and pump-probe measurements [20,25,26,29]. Studies on the (001) crystal surface focused on angle-resolved photoemis-
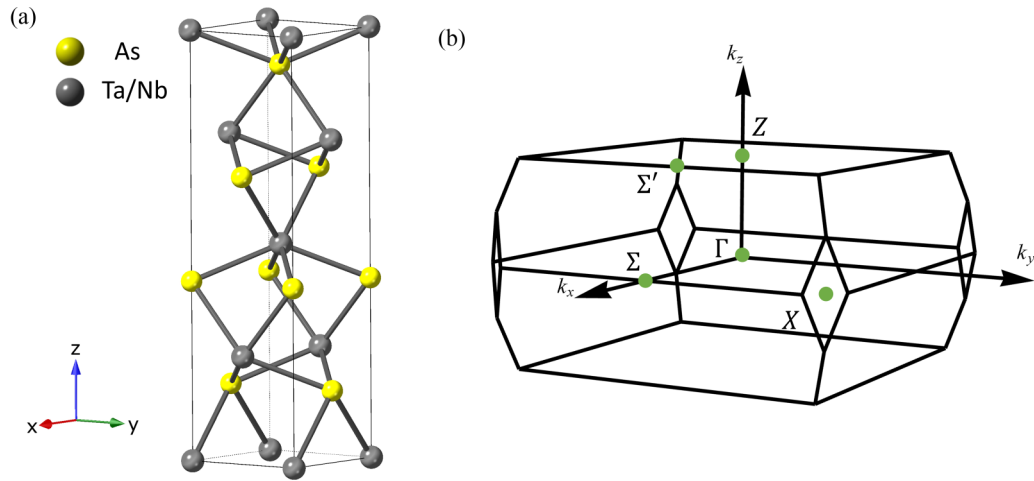
*gumq@sustech.edu.cn
†vxg8@psu.edu

FIG. 1. (a) Crystal structure of TaAs and NbAs. (b) The Brillouin zone and high-symmetry points of TaAs and NbAs.

sion spectroscopy and linear spectroscopy at low energies from 0 to 1 eV [2,7,23,30,31]. Linear spectroscopy and Raman studies also exist on (107) orientation [21,22]. In this paper, we use the (010) crystal plane, which allows us to directly probe properties along the principal axes [100] and [001] in the crystal plane and study the anisotropic linear optical properties and resonances in TaAs and NbAs. We also studied (112) planes to confirm the uniqueness of the measured dielectric function. Large anisotropic optical dielectric resonances are found <3.5 eV. The complete parameterized Lorentz oscillators within 1.2–6 eV [experiment (Expt.)] and 0–6 eV [density functional theory (DFT)] are reported, corresponding to interband transitions. Strong resonances are found <1 eV between the first two conduction and valence bands near the Fermi level, which originate from Ta ($5d$)-to-Ta ($5d$) and As ($4p$)-to-Ta ($5d$) transitions. Resonances are observed near the energies where previous optical SHG experiments were performed [25,26]; they are expected to enhance the SHG effect. The contribution to the dielectric function from a localized k space volume [∼0.0125% of the volume of the first Brillouin zone (BZ)] centered around the Weyl points is also quantified; we find that these contributions are <25% of the total dielectric function below 0.5 eV and are negligible at energies >1 eV, indicating low-energy optical probes are required to discern topological band features in the TaAs family.

II. METHODS

TaAs and NbAs exhibit a similar crystal structure [Fig. 1(a)] and the same point group 4*mm* ($a = 3.4348$ Å, $c = 11.641$ Å for TaAs; $a = 3.452$ Å, $c = 11.679$ Å for NbAs; the c axis in both cases is parallel to the [001] direction) [32,33]. Single crystals of TaAs and NbAs were grown by chemical vapor transport with stoichiometrically mixed Ta (or Nb) and As powders at ∼1000 °C for 4 wk (details can be found in Appendix E). As-grown surfaces of (020) were determined by $\theta - 2\theta$ x-ray diffraction (XRD), confirming single-crystalline properties and (020) out-of-plane direction (see Fig. 8). The in-plane [001] and [100] directions were then

determined by Laue backscattering diffraction and confirmed by the electron backscatter diffraction (EBSD; see Fig. 9).

Crystal quality plays a vital role in the intrinsic properties such as vacancies and stacking faults, which could shift the positions of Weyl nodes and alter the Fermi surface [34]. A previous study [35] showed that the Weyl nodes move closer to the Fermi level as the mobility increases. The quality of the studied crystals was examined using Hall measurements (Fig. 10). Analysis of the transport data show that the electron mobility of TaAs is $\mu_e(10\,\text{K}) = 6.04\,\text{m}^2\,\text{V}^{-1}\,\text{s}^{-1}$ and for the NbAs to be $\mu_e(10\,\text{K}) = 83.5\,\text{m}^2\,\text{V}^{-1}\,\text{s}^{-1}$, which is comparable with that reported in the literature [13,35–37]. Thus, the above properties suggest that the crystals studied here are reasonable representatives of the crystals reported in the literature.

Spectroscopic ellipsometry was performed using Woollam M-2000F focused beam spectroscopic ellipsometer with wavelengths from 1000 nm (1.2 eV) to 200 nm (6 eV). Amplitude change and phase shift of the specularly reflected light were collected as a function of the wavelength, which is sensitive to the crystal orientations. Three different orientations (see below) were measured and fitted simultaneously with the Lorentz model to confirm the uniqueness of the model. The complex dielectric permittivity tensor for the uniaxial system is given by the diagonal second rank tensor $\widetilde{\varepsilon} = (\tilde{\varepsilon}_{11} = \tilde{\varepsilon}_{22}, \tilde{\varepsilon}_{33})$, where subscripts 1 and 3 denote crystallographic a and c axes. The three different crystal cuts used in this study are represented as orientation A: [001]//lab x, [010]//lab z; orientation B: [001]//lab y, [010]//lab z; and orientation C: [1 −1 0]//lab x, (112)//lab z; respectively where the x-z plane is the plane of incidence. The Kramers–Kronig relationship between real and imaginary components of the dielectric tensor was imposed during the modeling of the ellipsometry data. The imaginary component of the dielectric function was forced to be positive in all the fittings.

DFT calculations were performed using the Vienna *Ab initio* Simulation Package (VASP) [38] to provide insights into the electronic properties leading to the optical dielectric function. The Perdew–Burke–Ernzerhof (PBE) functional [39] with spin-orbital coupling (SOC) interactions were used
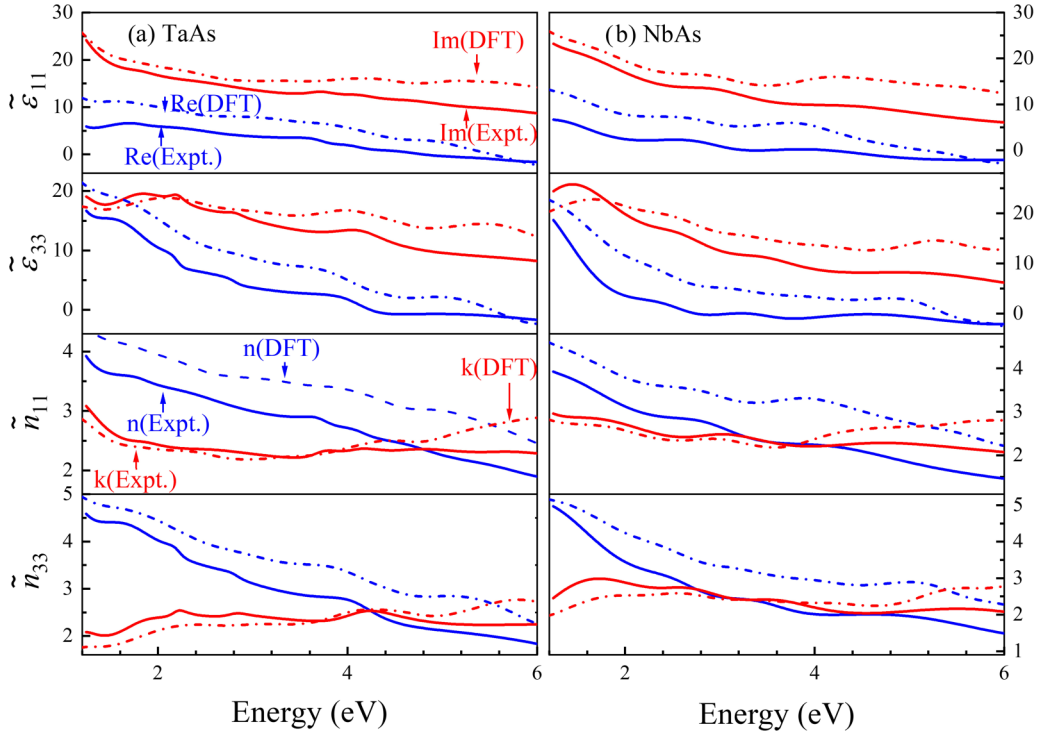
FIG. 2. The complex dielectric functions $\tilde{\varepsilon}_r$ and refractive indices $\tilde{n} = n + ik$ of (a) TaAs and (b) NbAs. The solid lines and dashed lines represent the experiment (Expt.) and density functional theory (DFT), respectively, with the smearing factor set to 0.2 eV. The blue and red curves are the real (Re) and imaginary (Im) components of the dielectric constant $\tilde{\varepsilon}$ and refractive index $\tilde{n}$. Subscripts 1 and 3 indicate directions along ordinary and extraordinary eigendirections.

in all calculations with a plane-wave expansion up to 500 eV. The projector-augmented wave (PAW) method [40] was used to treat the core and the valence electrons using the following electronic configurations: $5p^66s^25d^3$ for Ta, $4p^65s^24d^3$ for Nb, and $4s^24p^3$ for As. A $30 \times 30 \times 30$ Γ-centered Monkhorst-Pack k-point mesh was used for calculating the electron density of states (DOS) and the optical properties. Multiple smearing factors have been tested from 0.02 to 0.2 eV to find the best match to the experimental results. Two representative smearing factors (0.02 and 0.2 eV) were then evaluated, and since the results from the 0.2 eV smearing factor matched the experiments better, these are presented in the main text (see Figs. 12–13 and Tables V–VIII for results using a smearing factor of 0.02 eV). To evaluate the contribution of the dielectric function from the momentum space near the Weyl points, we used dense k-point grids and calculated the dielectric function contribution from a small volume $\frac{(\vec{b}_1 \times \vec{b}_2)\cdot\vec{b}_3}{20^3}$ centered around either WP1 or WP2. Note that $\vec{b}_1$, $\vec{b}_2$, and $\vec{b}_3$ are reciprocal lattice vectors for the primitive cell. Due to the metallic nature of TaAs and NbAs, an isotropic free carrier response [41] was also added to the calculated dielectric function, and the associated coefficients are included in Tables I–IV.

III. RESULTS AND DISCUSSION

A. Anisotropic dielectric tensor: experiments and DFT

The complex dielectric function $\tilde{\varepsilon}_r$ and refractive index $\tilde{n}$ obtained from both ellipsometry and DFT is shown in Fig. 2

(see Fig. 11 for a smearing factor of 0.02 eV). The experimental and DFT results show a reasonable agreement in terms of the trends, magnitudes, and resonance frequencies; this level of agreement between DFT and experiments is considered acceptable [42,43] because DFT is a zero-temperature theory and has a well-known underestimation of the energy of excited states. The plasma edge determined in previous studies is <0.1 eV [22,24]. Therefore, in the visible range, the dielectric function is dominated by interband transitions. Including the Drude behavior improves the agreement between DFT and experiments <~1.3 eV. To capture the resonances from 1.2 to 6 eV, the Lorentz model is used to simulate phase and intensity changes of the reflected light in the ellipsometry data as shown below [26]:

$$\tilde{\varepsilon} = \varepsilon_\infty + \sum_n^N \frac{A_n \Gamma_n E_n}{E_n^2 - E^2 - iE\Gamma_n} + \frac{A_{\mathrm{UV}}}{E_{\mathrm{UV}}^2 - E^2} + \frac{A_{\mathrm{IR}}}{E^2}, \quad (1)$$

where A_n, Γ_n, and E_n are the resonance amplitude, broadening, and energies, respectively, of each oscillator labeled by n, and ε_∞ represents the dielectric constant in the infinite frequency limit. Subscripts are used as deep-ultraviolet (UV) and infrared (IR) poles, respectively, beyond the fitting spectrum. In TaAs, eight oscillators are captured along the crystallographic a axis, and seven oscillators are captured along the c axis. The detailed fitting parameters for oscillators are shown in Table I (for the ordinary component) and Table II (for the extraordinary component) for TaAs, and in Table III (for the ordinary component) and Table IV (for the extraordinary component) for NbAs.
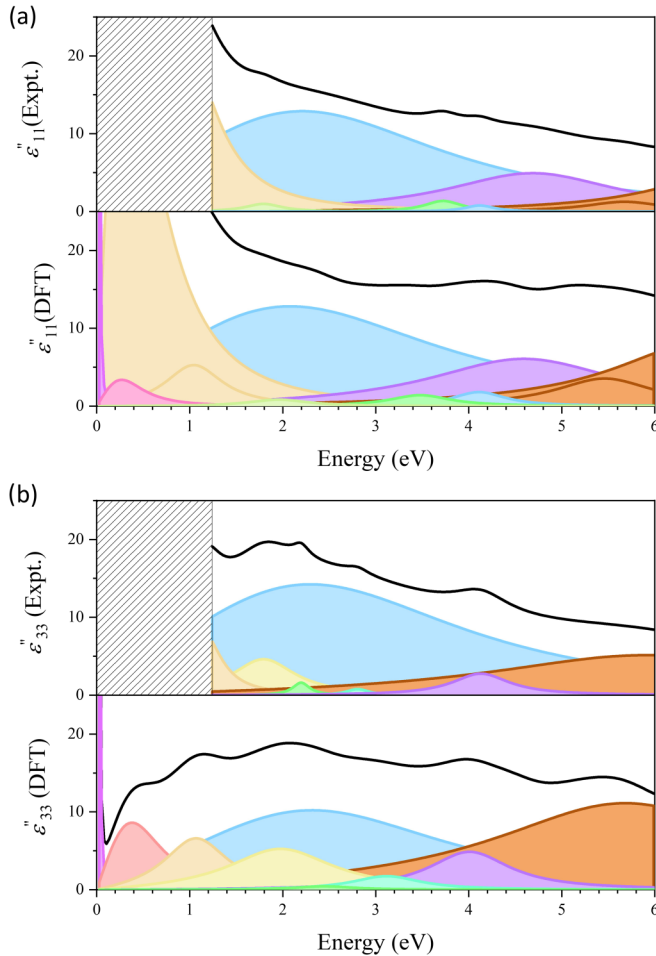
FIG. 3. Detailed Lorentz oscillators for TaAs obtained from both experiments and density functional theory (DFT) for a smearing factor of 0.2 eV. (a) Ordinary imaginary dielectric function ε_{11}''. The hatched area indicates the energy range beyond the experimentally measured spectrum. (b) Extraordinary imaginary dielectric function ε_{33}''. The black curve is the total imaginary dielectric function. Colored curves represent individual oscillators. In each subplot, similar colors of oscillators are approximate many-to-one mapping from theory to experiments; such mapping should not be strictly interpreted but only as a general guide to the eye, as described in the main text. The resonance energies and linewidths are given in Tables V and VI.

It is found that, within 1.2–6 eV, k decreases slower than n and gradually exceeds the real component. Thus, with an increase in the photon energy, the reflectivities of TaAs and NbAs decrease, in agreement with previous literature [22], while the absorption coefficients show much less dispersion with energy. However, near the measured spectrum edges (<1.2 eV and >6 eV), the oscillators are not fully captured in the experiments, and only the tails of resonances can be observed. Therefore, the resonance energies of the first and last oscillators along each of the eigendirections are set slightly beyond the experimentally measured spectrum to simulate the resonance near the spectral edges. The broadening parameters Γ_n in Eq. (1) show a similar magnitude between experiments and DFT for a smearing factor of 0.2 eV but are larger for the experimental resonances than for the DFT

resonances when using a smearing factor 0.02 eV. The larger smearing factor obscures the details of several narrower DFT resonances (seen with a smearing factor of 0.02 eV, as shown in Fig. 11). We consider the larger smearing factor to be a finite-temperature effect and the smaller smearing factor to be a low-temperature effect.

Having shown the overall agreement between experiments and theory in Fig. 2, and given that the DFT can shed light on the electronic transitions at energies of relevance, we next focus our discussions below on the DFT resonances. The linear dielectric functions from DFT are fitted from 0 to 6 eV using Eq. (1). The complete set of Expt. and DFT oscillators from 1.2 to 6 eV and 0 to 6 eV for TaAs are shown in Fig. 3 (see Fig. 6 for NbAs), and the detailed fitting parameters are shown in Tables I–IVI (results of the smearing factor set to 0.02 eV can be found in Appendix G). The black curve shows the total ε'', and the colored curves represent the fitted oscillators. Nine oscillators are fitted along the *a* direction, and eight oscillators are fitted along the *c* direction from 0 to 6 eV. The resonances captured by Expt. and DFT show an excellent qualitative match and a reasonable quantitative match. In Fig. 3(a), resonances in Expt. and DFT at similar energies are mapped with the same colors; this mapping should be taken as approximate guides to the eye and not as a strict many-to-one mapping. Along the ordinary direction, experimental oscillators at 1.0, 1.8, 2.9, 3.7, and 4.1 eV can be approximately one-to-one mapped with DFT oscillators at 1.1, 2.0, 2.8, 3.5, and 4.1 eV, respectively. Along the extraordinary direction, experimental oscillators at 1.2, 1.8, 2.2, 2.8, 3.0, and 4.1 eV can be one-to-one mapped to the DFT resonances at 1.2, 1.9, 2.2, 2.9, 3.1, and 4.1 eV, as shown in Fig. 3(b). A resonance dominates the dielectric constant at ~0.2 eV along the ordinary direction under a smearing factor of 0.02 eV [see Fig. 12(b)], which can be associated with transitions from the lower Weyl bands to the energy states above the upper Weyl bands at WP2; this resonance is obscured with a larger smearing factor.

B. Band structure and optical transitions

Since the optical excitation occurs across the bands throughout the entire BZ, both transitions from the nontopological bands and the topological (Weyl) bands are reflected in the total dielectric spectrum, and care is needed in distinguishing their independent contributions. To understand the optical dielectric functions plotted in Figs. 2 and 9, we carefully examine the electronic band structure and the optical transition matrix elements. With the confidence in the DFT calculated dielectric function based on its reasonable comparison with experiments (Fig. 2), we next proceed to look carefully at their microscopic origins.

In Fig. 4(a), the calculated DFT-SOC band structure and the resulting DOS for TaAs are shown (the corresponding figure for the band structure and the DOS for NbAs are shown in Fig. 7). In the figures, V1–V8 and C1–C8 are sequentially numbered valence and conduction bands, respectively. Two different Weyl points (WP1 and WP2) were previously identified to be located along the $\Gamma - \Sigma$ and $\Sigma - \Sigma_1$ directions highlighted in the dashed box, in the absence of SOC [see Fig. 1(b) for high-symmetry points] [2,3]. When SOC is considered, the lines of Weyl nodes are further decomposed into
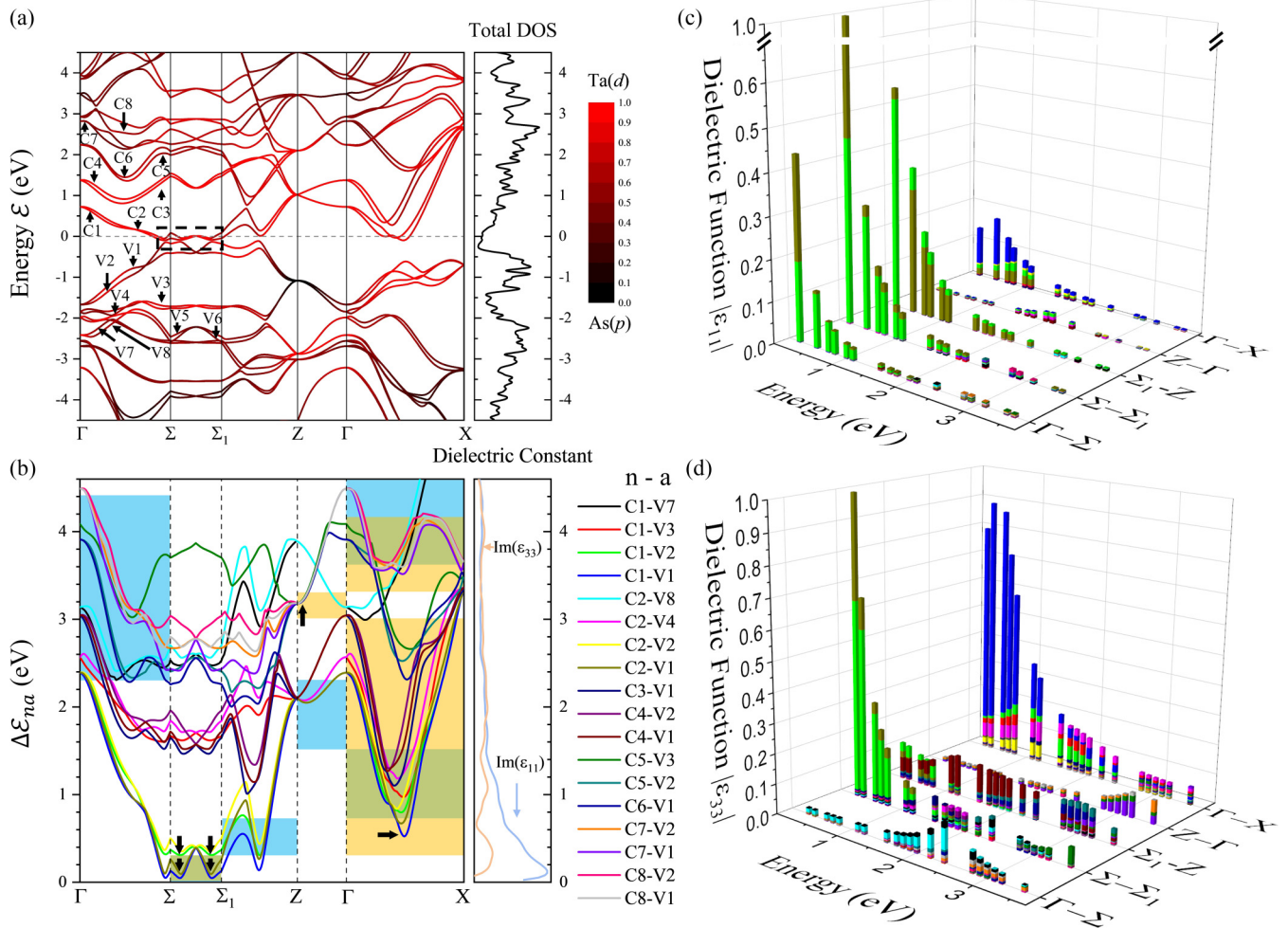
FIG. 4. (a) Density functional theory (DFT) spin-orbit coupling (SOC) band structure of TaAs. The color scale represents the relative band character of Ta (d) (red) vs As (p) (black) orbitals. Dashed rectangle highlights positions of Weyl points without SOC. (b) The energy difference $\Delta\mathcal{E}_{na}$ between selected pairs of bands (n,a) listed on the right contributing the most to the magnitude of the dielectric functions. The shaded areas highlight the paths and bands that contribute most to the dielectric function in that energy range. The blue, yellow, and green boxes correspond to pairs of bands contributing the most to $|\tilde{\varepsilon}_{11}|$, $|\tilde{\varepsilon}_{33}|$, and both, respectively. Arrows indicate Van Hove singularities that contribute to resonances. Normalized k-dependent contributions to the dielectric constants for the same pairs of bands as in (b) calculated along the (c) ordinary and (d) extraordinary directions, respectively, using Eq. (2). The color scale is the same as in (b). The smearing factor used for (b)–(d) is 0.2 eV.

12 pairs of Weyl nodes, four pairs of WP1, and eight pairs of WP2 [3]. Mirror symmetry protects each pair of Weyl points. The k-space momenta for WP1 and WP2 are calculated to be (0.015, 0.925, 0.004) and (0.505, 0.034, 0.313), where k_x, k_y, and k_z are parallel to the crystallographic a, b, and c axes, respectively. In the vicinity of the Fermi level, the states are mostly contributed by the hybridized Ta (d) orbital, while the states provided by As (p) are concentrated near the Z point. Deep within the valence band, the states are mostly As (p) character. The conduction band is mostly composed of Ta (d) orbitals. In the case of optical excitation in the IR and visible regimes, optical excitations in TaAs are dominated by Ta (d) to Ta (d) and As (p) to Ta (d) transitions. To evaluate major optical transitions that contribute to the macroscopic resonances, the energy difference $\Delta\mathcal{E}_{na}$ is shown in Fig. 4(b), where n and a represent a pair of bands, labeled n and a, as indicated in the legend next to the panel (b). For example, the red plot in panel (b) represents the energy difference between

the third valence band $a =$ V3 and the first conduction band $n =$ C1, as indicated in panel (a). Similarly, other pairs of bands are represented by other colors as indicated.

To connect the macroscopic Lorentz resonances with the optical transitions in the band structure, we then evaluate theoretical resonances and k-dependent direct transitions. Here, we focus on the oscillators <3.5 eV, where most experimental optical characterizations are performed. The linear spectroscopic susceptibility is determined by electric dipole transition moments and their resonant and antiresonant states expressed as [44]

$$\chi_{ij}^{(1)}(\omega)$$

$$= \frac{N}{\epsilon_0\hbar} \sum_k \sum_{(n,a)} \left[\frac{\mu_{an}^i \mu_{na}^j}{(\omega_{na} - \omega) - i\gamma_{na}} + \frac{\mu_{na}^j \mu_{an}^i}{(\omega_{na} + \omega) + i\gamma_{na}} \right],$$
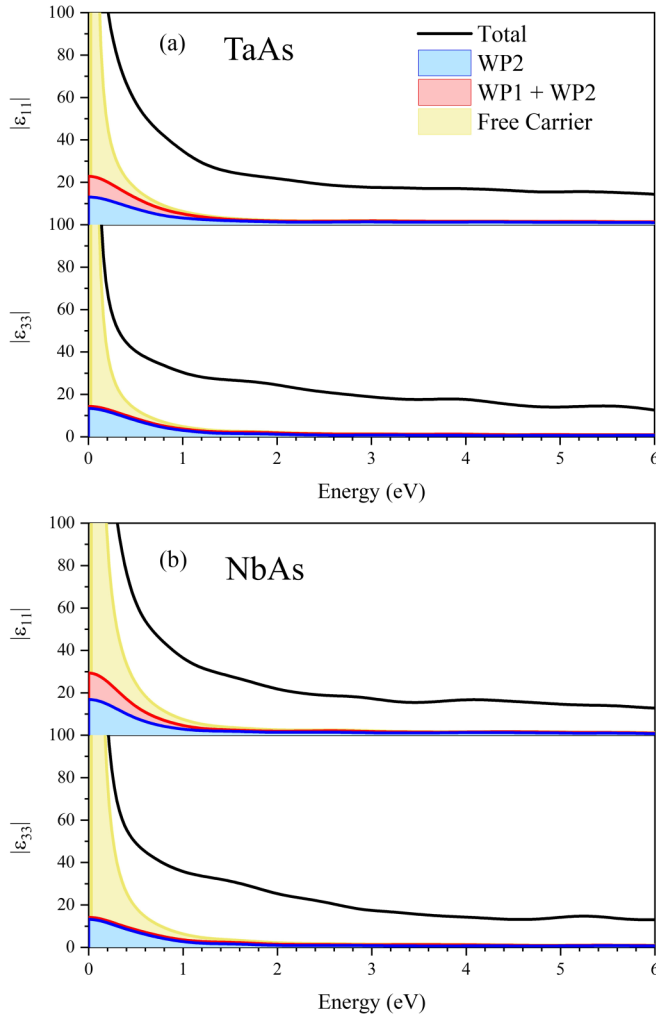
(2)

FIG. 5. Stacked plots of the contributions of a small k-space [0.0125% of the volume of the first Brillouin zone (BZ)] centered around the two types of Weyl points (WP1 and WP2), to the magnitudes of dielectric functions $|\tilde{\varepsilon}|$ for a smearing factor of 0.2 eV. (a) Dielectric functions of TaAs. (b) Dielectric functions of NbAs. The upper panel represents the ordinary direction, and the bottom panel represents the extraordinary direction. The black (entire BZ), red (k-space centered at 8 WP1 + 16 WP2), blue (k-space centered 16 WP2), and yellow (free carrier) curves represent $|\tilde{\varepsilon}|$ contributions, as noted from different regions of the BZ.

where $\omega_{na} = \omega_n - \omega_a = \Delta \mathcal{E}_{na}/\hbar$ between energy bands n and a, and $\chi_{ij}^{(1)}$, μ, ω, N, k, and γ are, respectively, the anisotropic susceptibility component (i and j are dummy variables representing directions), electric dipole transition moment, photon frequency, the number density of atoms, momentum space, and decay rate related to the damping term. Here, n and a represent the excited and ground states. In DFT, the damping factor was taken to be $\gamma_{na} = 0.2$ eV, the same as the smearing factor, as described earlier. The electric dipole transition moments μ_{na} were calculated by DFT for every pair of bands n and a at every point of the BZ in Fig. 4(a), i.e., $\mu_{na} \equiv f(n, a, k)$. To generate the total dielectric contribution for every energy shown on the right-hand-most panel in Fig. 4(b), we perform the summation over every pair of bands (n,a) at every k-point along the high-symmetry directions shown in

panel (a), as indicated in Eq. (2). The dominant contribution to the dielectric function at each energy $\hbar\omega$ comes from the pairs of bands n and a such that $\Delta \mathcal{E}_{na} \approx \hbar\omega$; these dominant regions in the k-space are shown in panel (b) with light blue, yellow, and green shaded rectangular regions. For example, the shaded blue box shown in the $\Gamma - \Sigma$ path indicates a dominant contribution from this path to the $|\tilde{\varepsilon}_{11}|$ in the energy range from 2.2 to 4.4 eV; the $\mathrm{Im}(\tilde{\varepsilon}_{11})$ is shown as a blue curve on the right to correspond to the blue rectangles on the left. Similarly, for example, the yellow rectangle boxes in the $\Gamma - X$ path indicate a dominant contribution from this path to the $|\tilde{\varepsilon}_{33}|$ in the energy range from 0.3 to 3 eV and 3.2 to 4.2 eV; the $\mathrm{Im}(\tilde{\varepsilon}_{33})$ is shown as a yellow curve on the right to correspond to the yellow rectangles on the left. Finally, the green rectangles (overlap of blue and yellow rectangles) in the left correspond to regions which contribute dominantly to both $|\tilde{\varepsilon}_{11}|$ and $|\tilde{\varepsilon}_{33}|$.

Panels (c) and (d) in Fig. 4 plot the dominant contributions to $|\tilde{\varepsilon}_{11}|$ and $|\tilde{\varepsilon}_{33}|$ with a finer momentum and energy resolution of the contributing bands. For example, the peak in panel (c) at 0.2 eV (the energy at the saddle point between the Weyl points) along the $\Sigma - \Sigma_1$ path indicates that this path contributes most strongly to the dielectric function $|\tilde{\varepsilon}_{11}|$. Further, this contribution comes from the pair of bands (V1, C2) and (V2, C1) as shown by the color coding of the bar chart at this location [the color code is given in panel (b)]; these are Ta $(5d)$-to-Ta $(5d)$ transitions. The results show that the dielectric contribution to $|\varepsilon_{11}|$ at 0.2 eV from the saddle point between the pair of Weyl points is dominated mostly by the $\Sigma - \Sigma_1$ path, followed by $\Sigma - Z$, and $\Gamma - \Sigma$ paths. From 0.3 to 0.7 eV, the k-space that contributes to $|\tilde{\varepsilon}_{11}|$ changes to $\Sigma_1 - Z$. Within 0.7–1.5 eV, various bands in the $\Gamma - X$ path dominate $|\tilde{\varepsilon}_{11}|$. The $Z - \Gamma$ path starts to play a significant role from 1.5 to 2.3 eV because of a collection of resonant bands near the high-symmetry Z point. In the energy range from 2.3 to 3.5 eV, the predominant k-space contribution to the dielectric function shifts to $\Gamma - \Sigma$ because of the large joint DOS (JDOS). Along the crystallographic c axis, the dielectric contribution to $|\tilde{\varepsilon}_{33}|$ at 0.2 eV is dominated mostly by the $\Sigma - \Sigma_1$ path, followed by $\Gamma - X$ path; the dominant contributing pairs of bands are (V1, C2), (V2, C1), and (V1, C1). At energy <0.3 eV, the optical transitions occur mostly along $\Sigma - \Sigma_1$. Within 0.3–3.0 eV and 3.3–4.1 eV, $\Gamma - X$ is the primary k-space path that dominates the $|\tilde{\varepsilon}_{33}|$, as shown in the blue and green rectangles in Fig. 4(b).

C. Resonances close to observed optical SHG energies

Since $\chi_{333}^{(2)}$ is proportional to the product $\tilde{\varepsilon}_{33}^2(\omega)\tilde{\varepsilon}_{33}(2\omega)$, and since resonances will enhance the linear dielectric permittivities, they will enhance $\chi_{333}^{(2)}$ [45]. A large $\chi_{333}^{(2)}$ can be observed by a large transition dipole moment μ for a linear resonance or a resonance close to either the ω or 2ω state [44]. Therefore, the direct optical transition with photon energy close to either the ω or 2ω state will enhance the SHG response. Optical SHG measurements were previously performed at various incident fundamental energies such as 0.7 and 1.55 eV, and large $\chi_{333}^{(2)}$ coefficients were reported [25,26]. Experimental oscillators at 1.2, 1.8, and 3.0 eV, and DFT oscillators at 0.5, 1.2, 1.9, and 3.1 eV are close to the

reported fundamental and SHG energies of interest and thus likely resonantly enhancing the SHG. The $\Gamma - X$ dominates the overall $|\tilde{\varepsilon}_{33}|$ from 0.5 to 3 eV away from momentum space where Weyl points reside, indicating the trivial bands are the major resonance source of large $|\tilde{\varepsilon}_{33}|$ instead of Weyl-related states. Major optical transitions occur between V1 and C1 along $\Gamma - X$ at 0.7 and 1.55 eV. It is worth noting that $Z - \Gamma$ exhibits large $|\tilde{\varepsilon}_{33}|$ between 3.0 and 3.3 eV due to resonating bands at high-symmetry Z points which are potentially resonant with the optical SHG experimentally observed at 3.1 eV in the previous literature [25,46]. In addition, there are contributions from Van Hove singularities (VHSs), and larger μ contributing (see next section) to the SHG enhancement at 3.1 eV energy. All these resonances can thus enhance the observed SHG.

D. VHSs and contributions from *k*-space in proximity to the Weyl points

A set of near-parallel flat bands or where there is a change in the slope of the $E(k)$ relation can produce VHSs that give rise to large JDOS [47–51]. The critical points in the band structure exhibiting VHSs have been previously reported at the saddle points connecting two Weyl nodes [23,52]. Along the extraordinary direction, the VHS is confirmed as highlighted by the dark arrows in Fig. 4(b) where $\nabla_k(\Delta\varepsilon_{na}) \approx 0$ [49,53]. Here, k is the lattice momentum, and $\Delta\varepsilon_{na}$ is the energy difference between band n and a. By identifying the k-space momenta, the VHSs are located at $\Sigma - \Sigma_1 < 0.4$ eV, at $\Gamma - X \sim 0.5$ eV, and near high-symmetry point Z at 3.1 eV. The resonances contributed by VHSs are confirmed by macroscopic oscillators at 0.5 and 3.1 eV. Moreover, the collection of bands near Z at 3.1 eV further increases the JDOS. In addition, the magnitudes of dipolar transition matrix elements are larger near those critical points. As for the parallel band (V1, C1) as highlighted in the dark arrow ~ 0.7 eV, the magnitudes of dipolar transition matrix elements show the largest value and are up to ~ 100 times larger than nearby momentum space. Near 1.55 eV, there is no VHS contributing along $\Gamma - X$, indicating the dielectric function at 1.55 eV is majorly contributed by direct optical transitions. Similarly, near the high-symmetry point Z, the magnitudes of dipolar transition matrix elements for the pair of bands (V1,C8), (V2, C7), and (V3, C5) dominate and are up to 85 times larger than the nearby momentum space; this enhancement directly contributes to the resonance at 3.1 eV and, hence, to the SHG detected at this energy. SHG is thus enhanced by direct optical transitions, VHSs, and large transition matrix elements.

Motivated by the resonances near the Weyl points, we then examine the contributions of the momentum space in the proximity of two different types of Weyl points to the dielectric functions. Figure 5 shows the anisotropic dielectric functions contributed by a small volume of k-space (which is 0.0125% of the volume of the first BZ) around WP1 and WP2. For simplicity, in the discussion below, we will simply call these contributions as those "due to WP1 and WP2." The free carrier contributions are also included for both TaAs and NbAs to fulfill the metallic properties [22,54,55]. Though interband transitions are significant $< 0.2–0.3$ eV, the free carrier contribution to the dielectric function dominates. Therefore, < 0.5

eV, the contributions from both WP1 and WP2 are $< 25\%$ of the total dielectric function in TaAs and NbAs.

Along the ordinary direction, both WP1 and WP2 show a similar contribution to $|\tilde{\varepsilon}_{11}|$ across the energy spectrum, and the magnitude of the dielectric functions tends to diminish after 0.2 eV. Along the extraordinary direction, the contribution to the $|\tilde{\varepsilon}_{33}|$ from WP2 tends to dominate over WP1, and the contribution is negligible > 1 eV. The DFT results in this paper agree well with previous conclusions performed in the low-energy range (0–0.2 eV) using a linear band approximation [24]. Below 0.2 eV, the remaining dielectric function other than contributions from WP1 or WP2 suggests they arise from dielectric resonances between trivial bands in both TaAs and NbAs. This anisotropic behavior in the lower energy range can be understood as different dispersions at two Weyl points using the approximate expression for the matrix elements for interband transitions $+k|p_j| - k^2 \propto \frac{1}{2}m^2(v_{F,+j}^2 + v_{F,-j}^2)$ [24]. Here, v_F, k, and p are Fermi velocity, wave vector, and transition dipole operator, respectively. Subscript j represents directions. Since the dispersion and Fermi velocity at WP2 along the polar axis is much larger than that of WP1, the dipolar transition matrix elements at WP2 are therefore larger, yielding a higher dielectric response along the polar axis. However, at higher energies, such as in the visible range where many optical measurements are typically performed, the contribution to dielectric function from both the Weyl points is negligible.

IV. CONCLUSIONS

The TaAs family has attracted tremendous interest since the discovery of Weyl semimetals. In this paper, we summarize the anisotropic dielectric functions of both TaAs and NbAs across a broad spectrum, combining ellipsometry and DFT. The magnitudes, trends, and resonance energy show an excellent match between experiments and theory. The energy-, momentum-, and band-resolved dielectric contributions clearly show resonance between trivial bands near the energies where giant SHG was reported earlier. Finally, we analyze the contribution of a small volume of k-space (0.0125% of the volume of the first BZ) centered around the WP1 and WP2 to the dielectric functions. It reveals that such a contribution is significant only < 0.5 eV and is $< 25\%$ of the total dielectric function; this contribution is insignificant > 1 eV, i.e., in the near-IR, visible, and the UV range. These results should provide guidance for future optical probing studies of Weyl physics in these important materials.
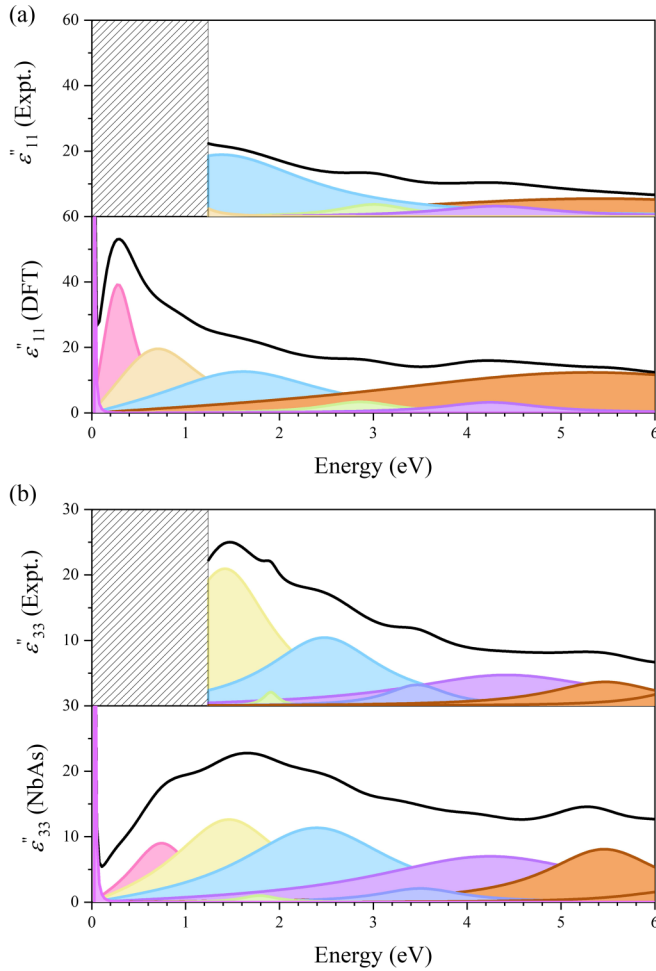
(a)

(b)

FIG. 6. Detailed Lorentz oscillators for NbAs obtained from both experiments and density functional theory (DFT) for a smearing factor of 0.2 eV. (a) Ordinary imaginary dielectric function ε''_{11}. The hatched area indicates the energy range beyond the experimentally measured spectrum. (b) Extraordinary imaginary dielectric function ε''_{33}. The black curve is the total imaginary dielectric function. Colored resonance fits represent individual oscillators. In each subplot, similar colors of oscillators are approximately many-to-one mapping from theory to experiments; they are only to be taken as a guide to the eye. The resonance energies and linewidths are given in Tables VII and VIII.

APPENDIX A: PARAMETERS OF LORENTZ OSCILLATORS FROM ELLIPSOMETRY AND DFT

Based on Eq. (1), parameters of oscillators in TaAs and NbAs are extrapolated and summarized in Tables I–IV. The spectroscopic range of ellipsometry covers the oscillators from 1.2 to 6 eV (1000–200 nm). The oscillators from DFT (for a smearing factor of 0.2 eV) are fitted from 0 to 6 eV to obtain a complete spectroscopic range and to compare with the experimental results.

TABLE I. Parameters for the Lorentz oscillators given by Eq. (1) and the Drude model for the ordinary dielectric function $|\bar{\varepsilon}_{11}|$ for TaAs. $\varepsilon^\infty = 1.8$ (Expt.) and 1.6 (DFT), $A_{UV} = 0.1$ (Expt). and 4.0 (DFT), $E_{UV} = 6.6$ (Expt.) and 7.0 (DFT), $A_{IR} = 10.0$ (Expt.), $\sigma_D = 2 \times 10^6$ ohm^{-1} m^{-1}, $\tau_D = 3.3$ ps [22]. A DFT smearing factor of 0.2 eV was used.

Oscillators (n)	Expt. E_n (Γ_n) (eV)	Expt. A_n (a.u.)	DFT E_n (Γ_n) (eV)	DFT A_n (a.u.)
1	1.0 (0.8)	21.2	0.5 (1.1)	40.3
2	1.8 (0.5)	1.0	1.1 (0.8)	5.6
3	2.9 (4.0)	11.3	2.0 (0.8)	0.9
4	3.7 (0.5)	1.4	2.8 (4.3)	11.1
5	4.1 (0.4)	0.8	3.5 (0.8)	1.4
6	4.8 (2.2)	4.9	4.1 (0.7)	1.8
7	5.7 (1.0)	1.2	4.8 (2.5)	6.0
8	6.8 (2.0)	4.6	5.5 (1.3)	3.5
9	–	–	6.6 (2.3)	8.1

APPENDIX B: ANISOTROPIC DIELECTRIC TENSOR IN NbAs: EXPERIMENTS AND DFT

Figure 6 shows the complete set of Expt. and DFT oscillators from 1.2 to 6 eV and 0 to 6 eV in NbAs. The black curve shows the total ε'', and the colored curves represent each oscillator. Like TaAs, six oscillators are fitted along the *a* direction, and nine oscillators are fitted along the *c* direction for DFT from 0 to 6 eV. Strong resonances can be identified in the low-energy range, which can be associated with the interband transitions near the Weyl points [56]. Figure 6(a) shows Expt. and DFT resonances in NbAs along the ordinary direction, and similar resonances are mapped with the same colors purely as an approximate guide to the eye. Experimental oscillators at 1.1, 1.7, 3.0, and 4.4 eV can be approximately mapped one-to-one with DFT oscillators at 0.9, 1.9, 2.9, and 4.3 eV. Figure 6(b) shows oscillators along the extraordinary direction. Resonances (Expt.) at 1.5, 1.9, 2.6, 3.5, and 4.6 eV can be relatively mapped one-to-one with DFT oscillators at 1.6, 1.8, 2.6, 3.5, and 4.5 eV, respectively.

TABLE II. Parameters for the Lorentz oscillators given by Eq. (1) and the Drude model for the extraordinary dielectric function $|\bar{\varepsilon}_{33}|$ for TaAs. $\varepsilon^\infty = 1.7$ (Expt.) and 1.6 (DFT), $A_{UV} = 0.1$ (Expt.) and ~ 0 (DFT), $E_{UV} = 6.5$ (Expt.) and 6.7 (DFT), $A_{IR} = 6.6$ (Expt.), $\sigma_D = 2 \times 10^6$ ohm^{-1} m^{-1}, $\tau_D = 3.3$ ps [22]. A DFT smearing factor of 0.2 eV was used.

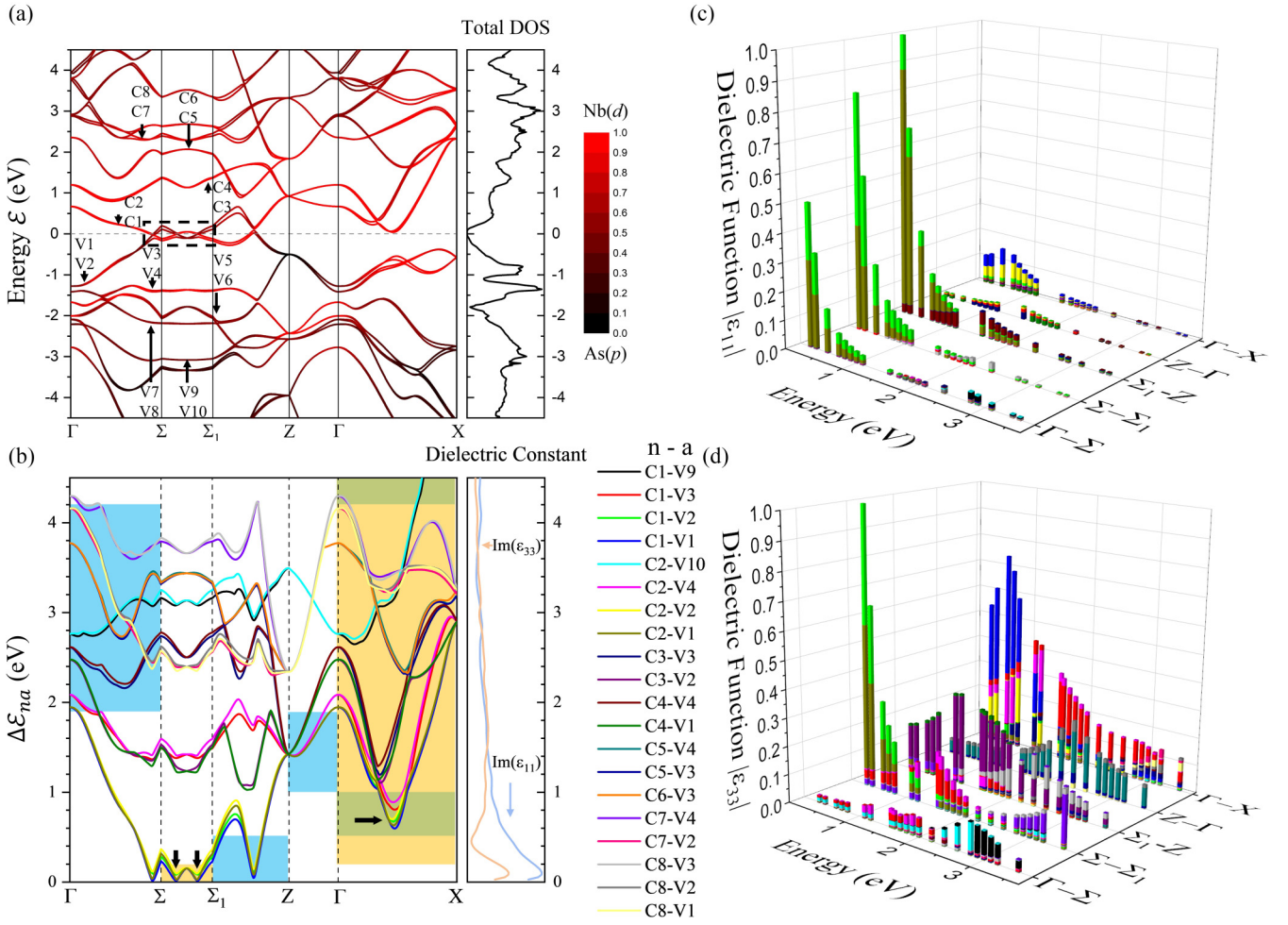| Oscillators (n)	Expt. E_n (Γ_n) (eV)	Expt. A_n (a.u.)	DFT E_n (Γ_n) (eV)	DFT A_n (a.u.)
1	1.2 (0.5)	8.0	0.5 (0.9)	7.0
2	1.8 (0.8)	4.6	1.2 (0.9)	6.2
3	2.2 (0.2)	1.6	1.9 (0.8)	2.5
4	2.8 (0.3)	0.8	2.2 (0.5)	1.1
5	3.0 (4.4)	12.4	2.9 (0.3)	0.04
6	4.1 (0.8)	2.8	3.1 (4.1)	12.2
7	6.2 (4.1)	5.0	4.1 (0.9)	3.5
8	–	–	6.1 (3.6)	10.0

FIG. 7. (a) Density functional theory (DFT) spin-orbit coupling (SOC) band structure of NbAs. The color scale represents the relative band character of Ta (*d*) (red) vs As (*p*) (black) orbitals. Dashed rectangle highlights positions of Weyl points without SOC. (b) The energy difference $\Delta\mathcal{E}_{na}$ between selected pairs of bands (*n,a*) listed on the right contributing the most to the magnitude of the dielectric functions. The shaded areas highlight the paths and bands that contribute most to the dielectric function in that energy range. The blue, yellow, and green boxes correspond to pairs of bands contributing the most to $|\tilde{\varepsilon}_{11}|$, $|\tilde{\varepsilon}_{33}|$, and both, respectively. Arrows indicate Van Hove singularities that contribute to resonances. Normalized *k*-dependent contributions to the dielectric constants for the same pairs of bands as in (b) calculated along the (c) ordinary and (d) extraordinary directions, respectively using Eq. (2). The color scale is the same as in (b). The smearing factor used for (b)–(d) is 0.2 eV.

TABLE III. Parameters for the Lorentz oscillators given by Eq. (1) and the Drude model for the ordinary dielectric function $|\tilde{\varepsilon}_{11}|$ for NbAs. $\varepsilon^\infty = 1.4$ (Expt.) and 0.01 (DFT), $A_{UV} = 1.4$ (Expt.) and 8.3 (DFT), $E_{UV} = 6.7$ (Expt.) and 7.0 (DFT), $A_{IR} = 12.2$ (Expt.), $\sigma_D = 1 \times 10^7$ ohm^{-1} m^{-1}, $\tau_D = 7.1$ ps [54,55]. A DFT smearing factor of 0.2 eV was used.

Oscillators (n)	Expt. E_n (Γ_n) (eV)	Expt. A_n (a.u.)	DFT E_n (Γ_n) (eV)	DFT A_n (a.u.)
1	1.1 (0.2)	11.3	0.3 (0.4)	35.3
2	1.7 (2.4)	17.3	0.9 (1.2)	17.4
3	3.0 (0.9)	3.4	1.9 (2.1)	11.7
4	4.4 (1.5)	2.6	2.9 (1.0)	3.3
5	5.9 (5.6)	5.1	4.3 (1.3)	3.2
6	–	–	6.0 (5.8)	11.6

TABLE IV. Parameters for the Lorentz oscillators given by Eq. (1) and the Drude model for the extraordinary dielectric function $|\tilde{\varepsilon}_{33}|$ for NbAs. $\varepsilon^\infty = 2.3$ (Expt.) and 1.0 (DFT), $A_{UV} = 3.4$ (Expt.) and 64.9 (DFT), $E_{UV} = 6.7$ (Expt.) and 7 (DFT), $A_{IR} = 8.3$ (Expt.), $\sigma_D = 1 \times 10^7$ ohm^{-1} m^{-1}, $\tau_D = 7.1$ ps [54,55]. A DFT smearing factor of 0.2 eV was used.

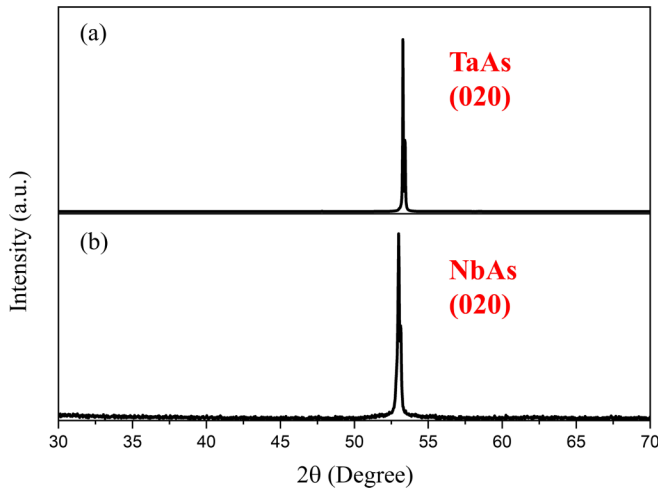| Oscillators (n)	Expt. E_n (Γ_n) (eV)	Expt. A_n (a.u.)	DFT E_n (Γ_n) (eV)	DFT A_n (a.u.)
1	1.5 (1.2)	20.1	0.3 (0.2)	2.0
2	1.9 (0.2)	1.9	0.8 (0.8)	8.5
3	2.6 (1.5)	10.2	1.6 (1.4)	12.0
4	3.5 (0.7)	3.0	1.8 (0.5)	1.0
5	4.6 (2.8)	4.7	2.6 (2.0)	11.0
6	5.5 (0.8)	3.5	3.5 (1.1)	2.1
7	6.4 (1.0)	2.9	4.5 (3.0)	6.8
8	–	–	5.5 (1.5)	8.1
9	–	–	6.3 (1.3)	1.8

FIG. 8. X-ray diffraction (XRD) of TaAs (020) and NbAs (020) plane. (a) Experimental XRD of the TaAs (020) peak. (b) Experimental XRD of NbAs (020) peak.

APPENDIX C: BAND STRUCTURE, BAND- AND MOMENTUM-RESOLVED DIELECTRIC RESPONSE IN NbAs

In Fig. 7(a), the calculated DFT-SOC band structure and the resulting DOS for NbAs are shown. V1–V10 and C1–C8 are sequentially numbered valence and conduction bands. The band splitting by SOC in NbAs is smaller than TaAs due to the smaller atomic number of Nb [57]. The k-space momenta for WP1 and WP2 are calculated to be (0.891, 0.005, 0) and (0.012, 0.503, 0.306), respectively. Near the Fermi level, the states are mostly contributed by the hybridized Nb (d) orbitals. Deep within the valence state, the states are mostly dominated by the As (p) orbitals. In the case of optical excitation in the IR and visible regimes, optical excitations in the

system are dominated by Nb (d)-to-Nb (d) and As (p)-to-Nb (d) transitions.

Figure 7(b) shows the energy difference $\Delta \varepsilon_{na}$ between pairs of bands contributing most to the dielectric function using Eq. (2). The colored rectangles show the momentum space and pairs of bands that predominantly contribute to a certain dielectric constant value using the same scheme presented in Fig. 4(b). In the Figs. 7(c) and 7(d), the dominant pairs of bands that contribute to $|\tilde{\varepsilon}_{11}|$ and $|\tilde{\varepsilon}_{33}|$ are shown, with a finer momentum and energy-resolved picture.

Along the ordinary direction, from 0 to 0.5 eV, the optical transitions mainly arise from $\Sigma_1 - Z$. Further, this contribution mainly comes from the pairs of bands (V1, C2) and (V2, C1), which mostly originate from Nb (d)-to-Nb (d) and As (p)-to-Nb (d) transitions. From 0.5 to 1 eV, the k-space that contributes predominantly to $|\tilde{\varepsilon}_{11}|$ changes to $\Gamma - X$. Here, $Z - \Gamma$ becomes significant from 1 to 1.9 eV because of a cluster of resonant bands near the high-symmetry Z point, which corresponds to the macroscopic resonance (DFT) at 1.6 eV. In the energy range from 1.9 to 4.2 eV, the predominant k-space shifts to $\Gamma - \Sigma$. Similarly, along the extraordinary direction of NbAs, the optical transitions <0.2 eV mainly arise from $\Sigma - \Sigma_1$ near the Weyl nodes without SOC [3]. In this energy range, the primary optical transitions are identified to be (V2, C1), (V1, C2), and (V1, C1). In the 0.2–4.5 eV range, $\Gamma - X$ is the primary k-space that dominates the $|\tilde{\varepsilon}_{33}|$.

APPENDIX D: RESONANCES NEAR OBSERVED SHG ENERGIES AND VHS IN NbAs

By examining resonances near 0.7, 1.55, and 3.1 eV along the extraordinary direction, experimental oscillators at 1.5 and 2.6 eV are close to the energies of interest. DFT oscillators at 0.8, 1.6, and 2.6 eV are near the reported energies. The $\Gamma - X$ path dominates the overall $|\tilde{\varepsilon}_{33}|$ at energies of interest, away from the Weyl points. The primary optical transition occurs

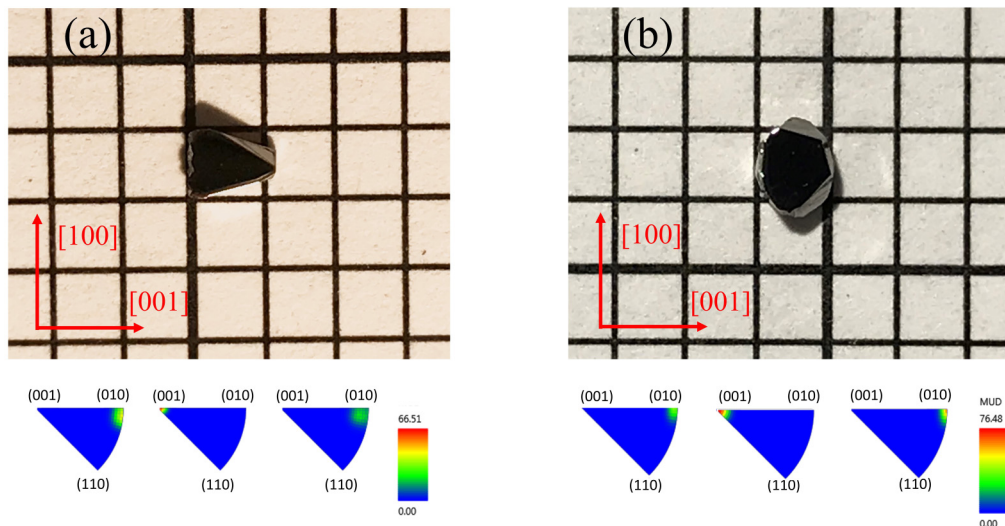FIG. 9. Optical images and inverse pole figures of synthesized (a) TaAs and (b) NbAs. The upper panel is the optical image of the studied crystals. The red arrows indicate crystallographic orientations. The size of the square boxes in the background is 2×2 mm. The bottom panel is the inverse pole figures obtained from the electron backscatter diffraction (EBSD). The out-of-plane direction is along [010].
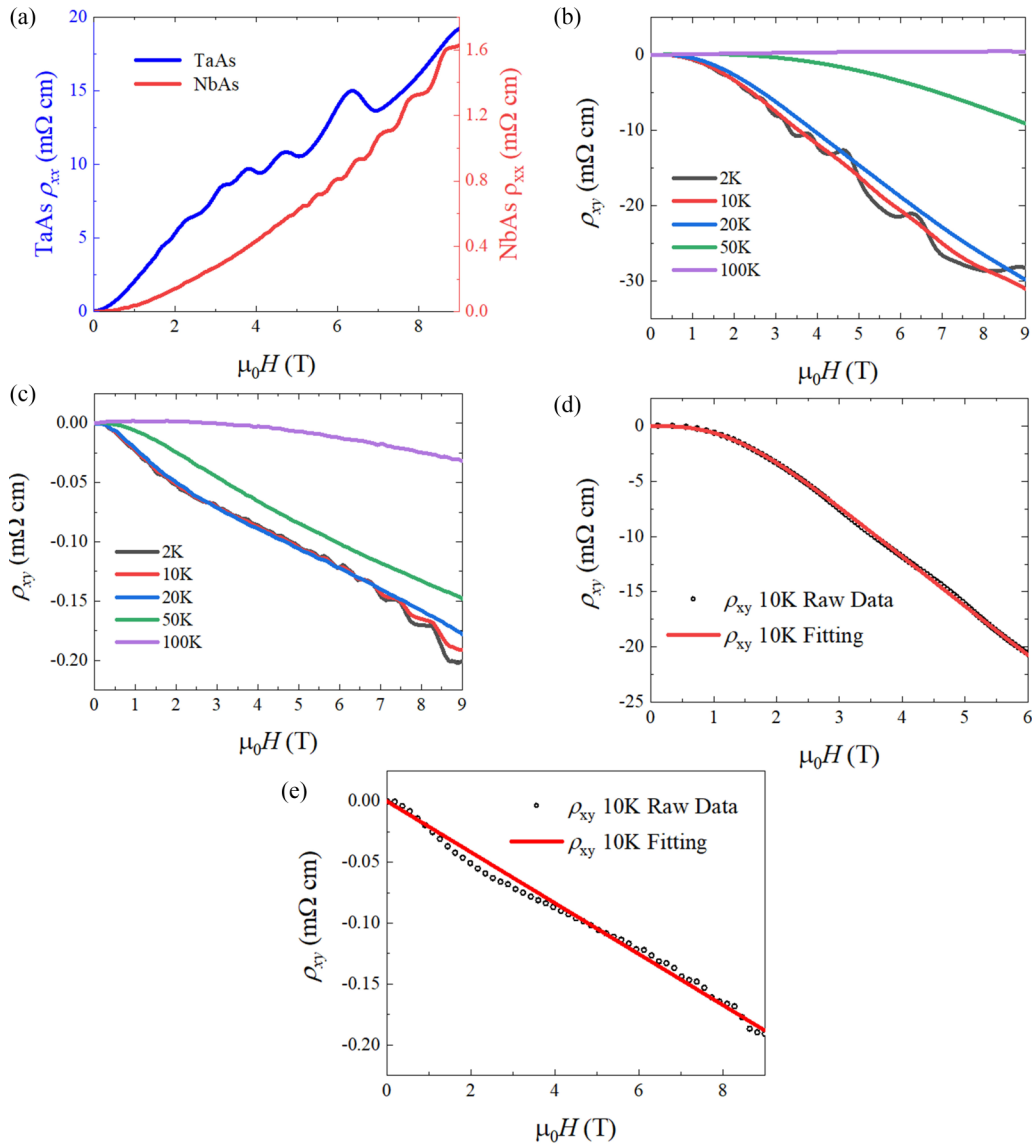
FIG. 10. Transport properties of TaAs and NbAs. (a) The magnetic field dependent longitudinal resistivity of TaAs and NbAs at 2 K. The Hall resistivity vs magnetic fields and 50 to 2 K in (b) TaAs and (c) NbAs. (d) The two-band model fitting of Hall resistivity for TaAs at 10 K. (e) The single-band model fitting of Hall resistivity of NbAs at 10 K.

between V1 and C1 along $\Gamma - X$ at 0.7 eV. At 1.55 eV, the major optical transitions are V4–C2 and V3–C1. Therefore, the enhancement at 1.55 eV is significantly contributed by the $\Gamma - X$ path. At 3.1 eV, more bands are involved in the optical transitions, while V2–C7 and V4–C2 contribute more to the dielectric function than the contribution from other transitions.

Like TaAs, VHS contributes to resonances along the extraordinary direction, as highlighted by the black arrows in Fig. 7(b). Below 0.2 eV, VHS can be observed at $\Sigma - \Sigma_1$. Near 0.7 eV, where SHG measurements were performed in this family, VHS at $\Gamma - X$ is expected to enhance the SHG response. Moreover, the dipole moments μ at the energy location of the dark arrows are larger than the rest of the k-space. Therefore, direct optical transitions, VHSs, and large dipolar transition matrix elements can enhance $|\tilde{\varepsilon}_{33}|$ and further increase the response near the fundamental and SHG energies.

APPENDIX E: SYNTHESIS AND STRUCTURAL CHARACTERIZATION

Single crystals of TaAs and NbAs were grown by chemical vapor transport. The stoichiometric ratio of Ta (Nb) and As powder was thoroughly mixed, pressed into a pellet, and sealed under a third atmospheric pressure of Ar in a quartz tube for the solid-state reaction. The tube was heated to 600 °C at 50 °C/h, stayed for 10 h, then heated to 1100 °C at 50 °C/h, and finally dwelled for another 10 h before water quenching. Three grams of such precursors were loaded with iodine pieces in a quartz tube. The density of the iodine was 18 mg/cm³. The quartz ampule was sealed under vacuum and put in a three-zone furnace for a 4-wk-long chemical vapor transport growth. The temperature was set to be 1050 °C (950 °C) at the source end and 950 °C (850 °C) at the sink end for TaAs (NbAs). Powder x-ray data were collected using a
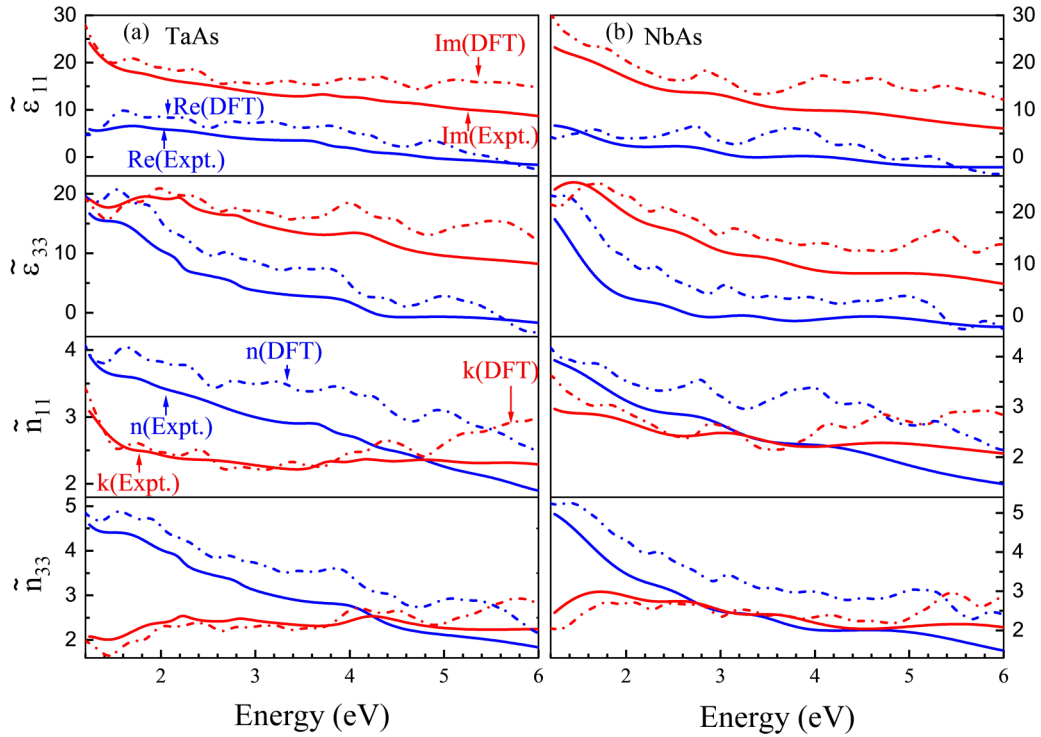
FIG. 11. The complex dielectric functions $\tilde{\varepsilon}_r$ and refractive indices $\tilde{n} = n + ik$ of (a) TaAs and (b)NbAs. The solid line and dashed line represent the experiment (Expt.) and density functional theory (DFT) with the smearing factor 0.02 eV, respectively. The blue and red curves are the real (Re) and imaginary (Im) components of the dielectric constant $\tilde{\varepsilon}$ and refractive index $\tilde{n}$. Subscripts 1 and 3 indicate directions along ordinary and extraordinary eigendirections.

PANalytical Empyrean diffractometer with Cu-Kα radiation. As-grown surfaces of (020) can be identified and confirmed with XRD, which was polished to a larger size using 1-μm sandpapers and later used for the spectroscopic study.

Single crystalline TaAs and NbAs are confirmed using θ-2θ XRD, as shown in Fig. 8. The out-of-plane direction is confirmed to be (020).

The orientations of the crystals were determined by combining Laue x-ray backscatter diffraction and EBSD. The raw crystals are shown in the upper panel of Fig. 9. By orientating the crystal axis parallel to the *x-y-z* coordinates (*z* as out-of-plane direction) in the EBSD system, the orientation maps are obtained with (020) intensity peaks along the *z* direction, confirming the previous XRD pattern in Fig. 8. The [001] direction peaks along *y* for TaAs and *x* for NbAs. The orientations are identified and aligned correctly for further anisotropic characterization.

APPENDIX F: TRANSPORT CHARACTERIZATION

To characterize the quality of studied crystals, electrical and magnetoelectrical transport measurements were conducted with a standard four-probe method in a Quantum Design Physical Property Measurement System. The electric current was applied within the plane, while the magnetic field was along the out-of-plane direction for both TaAs and NbAs. To eliminate the nonsymmetricity of the contacts, the longitudinal resistivity (ρ_{xx}) and Hall resistivity (ρ_{xy}) are symmetrized using the formulas $\rho_{xx}(H) = [\rho_{xx}(H) + \rho_{xx}(-H)]/2$ and

$\rho_{xy}(H) = [\rho_{xy}(H) - \rho_{xy}(-H)]/2$, respectively, where H is the magnetic field.

The magnetic field dependent longitudinal resistivities of TaAs and NbAs are shown in Fig. 10(a). In the low-temperature range ($<$100 K), Hall resistivity [Fig. 10(b) for TaAs; Fig. 10(c) for NbAs] shows large negative values, nonlinear field dependences, and Shubnikov–de Haas (SdH) oscillations, indicating both electrons and holes are involved in transport, and electrons make dominant contributions to transport. SdH oscillations are clearly observed at 2 K in both field sweep measurements of longitudinal and Hall resistivity, shown in Figs. 10(a)–10(c).

For TaAs, we have estimated the carrier densities and mobilities of low temperatures through the fits of longitudinal and Hall resistivity at 10 K by a two-band model: $n_e(10$ K$) = 7.12 \times 10^{23}$ m^{-3} and $n_h(10$ K$) = 5.56 \times 10^{23}$ m^{-3}, and mobilities $\mu_e(10$ K$) = 6.04$ m^2 V^{-1} s^{-1} and $\mu_h(10$ K$) = 2.54$ m^2 V^{-1} s^{-1}. All results above are comparable with previously reported data of TaAs single crystals [13,35,36]. In NbAs, strong SdH oscillation is also observed. Compared with TaAs, the Hall signal of NbAs at 2 K is more linear and can be analyzed by a single-band model. Similar to the previous report [37], the electron carrier density and electron mobility of the NbAs crystal is $n_e(10$ K$) = 2.7 \times 10^{25}$ m^{-3} and $\mu_e(10$ K$) = 83.5$ m^2 V^{-1} s^{-1}, respectively.

The fitting of TaAs transport data is presented in Fig. 10(d). The fitting of the low-temperature magnetoelectrical transport data is based on a simplified two-band model, where only one electron band and one hole band are considered. The
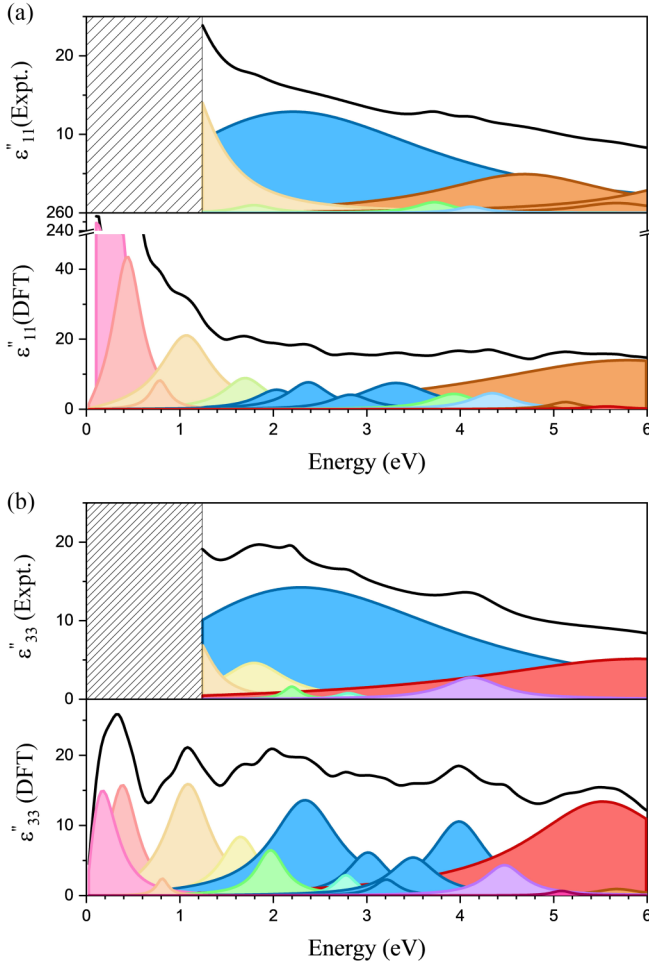
FIG. 12. Detailed Lorentz oscillators for TaAs obtained from both experiments and density functional theory (DFT) for a smearing factor of 0.02 eV. (a) Ordinary imaginary dielectric function ε''_{11}. The hatched area indicates the energy range beyond the experimentally measured spectrum. (b) Extraordinary imaginary dielectric function ε''_{33}. The black curve is the total imaginary dielectric function. Colored curves represent individual oscillators. In each subplot, similar colors of oscillators are approximate many-to-one mapping from theory to experiments; such mapping should not be strictly interpreted but only as a general guide to the eye, as described in the main text. The resonance energies and linewidths are given in Tables V and VI.
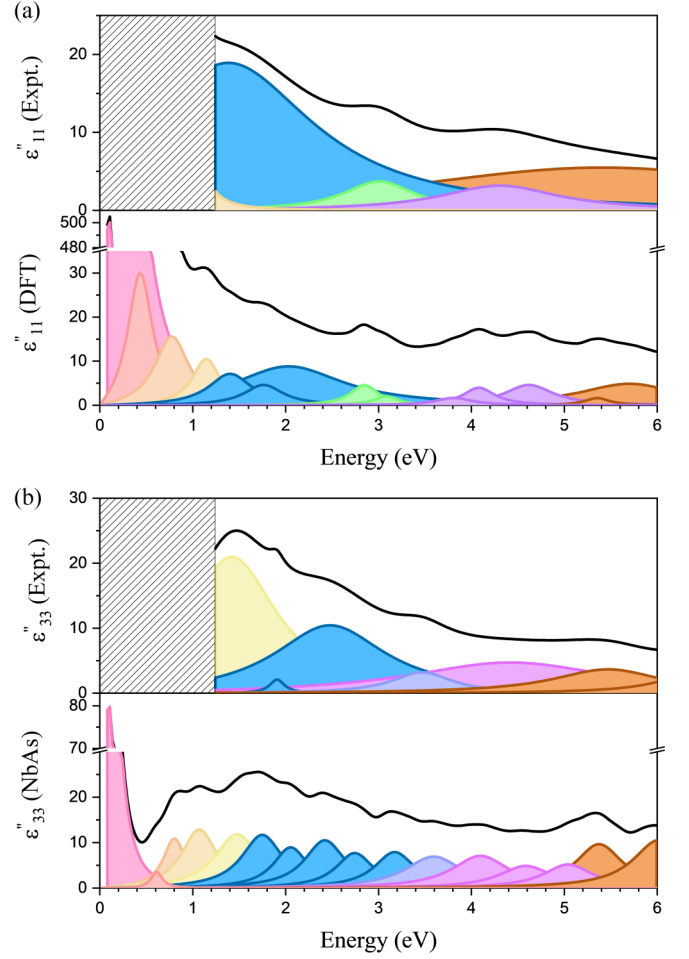
FIG. 13. Detailed Lorentz oscillators for NbAs obtained from both experiments and density functional theory (DFT) for a smearing factor of 0.02 eV. (a) Ordinary imaginary dielectric function ε''_{11}. The hatched area indicates the energy range beyond the experimentally measured spectrum. (b) Extraordinary imaginary dielectric function ε''_{33}. The black curve is the total imaginary dielectric function. Colored resonance fits represent individual oscillators. In each subplot, similar colors of oscillators are approximately many-to-one mapping from theory to experiments; they are only to be taken as a guide to the eye. The resonance energies and linewidths are given in Tables VII and VIII.

longitudinal resistivity (ρ_{xx}) and transverse resistivity (ρ_{xy}) can be described as [58]

$$\rho_{xx} = \frac{(n_e\mu_e + n_h\mu_h) + (n_e\mu_e\mu_h^2 + n_h\mu_h\mu_e^2)B^2}{(n_e\mu_e + n_h\mu_h)^2 + \mu_h^2\mu_e^2(n_h - n_e)^2B^2}\frac{1}{e}, \quad \text{(F1)}$$

$$\rho_{xy} = \frac{(n_h\mu_h^2 - n_e\mu_e^2) + \mu_h^2\mu_e^2(n_h - n_e)B^2}{(n_e\mu_e + n_h\mu_h)^2 + \mu_h^2\mu_e^2(n_h - n_e)^2B^2}\frac{B}{e}, \quad \text{(F2)}$$

where n_e (n_h) and μ_e (μ_h) are the density and mobility of the electron (hole) band, respectively. To constrain the freedom of the fitting, in this paper, the relationship between n_e and n_h is estimated by the linear fitting of the ρ_{xy} in the high-field range as $\rho_{xy} = \frac{1}{n_h - n_e}\frac{B}{e}$ [35]. The fitting of NbAs transport data is presented in Fig. 10(e). The fitting of the low-temperature magnetoelectrical transport data of NbAs is based on a sin-

gle band approximation. The carrier density is described by $n = \frac{1}{eR_H}$, where R_H is the Hall coefficient. The mobility is further given by $\mu = \frac{1}{en\rho_{xx}(0T)}$, where $\rho_{xx}(0T)$ is the longitudinal resistivity at zero magnetic field.

APPENDIX G: A CASE STUDY FOR A SMEARING FACTOR OF 0.02 eV

Based on Eq. (1), parameters of oscillators in TaAs and NbAs are extrapolated and summarized in Tables V–VIII for a smearing factor 0.02 eV. The spectroscopic range of ellipsometry covers the oscillators from 1.2 to 6 eV (1000–200 nm). The oscillators from DFT are fitted from 0 to 6 eV to obtain a complete spectroscopic range and to compare with the experimental results.

TABLE V. Parameters for the Lorentz oscillators given by Eq. (1) for the ordinary dielectric function $|\tilde{\varepsilon}_{11}|$ for TaAs. $\varepsilon^\infty = 1.8$ (Expt.) and 1.8 (DFT), $A_{\mathrm{UV}} = 0.1$ (Expt.) and 34.5 (DFT), $E_{\mathrm{UV}} = 6.6$ (Expt.) and 7.0 (DFT), $A_{\mathrm{IR}} = 10.0$ (Expt.). A DFT smearing factor of 0.02 eV was used.

Oscillators (n)	Expt. E_n (Γ_n) (eV)	Expt. A_n (a.u.)	DFT E_n (Γ_n) (eV)	DFT A_n (a.u.)
1	1.0 (0.8)	21.2	0.2 (0.3)	200.7
2	1.8 (0.5)	1.0	0.5 (0.4)	41.9
3	2.9 (4.0)	11.3	0.8 (0.2)	8.2
4	3.7 (0.5)	1.4	1.1 (0.7)	20.9
5	4.1 (0.4)	0.8	1.7 (0.6)	9.0
6	4.8 (2.2)	4.9	2.1 (0.6)	6.1
7	5.7 (1.0)	1.2	2.4 (0.5)	7.9
8	6.8 (2.0)	4.6	2.8 (0.5)	4.3
9	–	–	3.4 (1.0)	9.3
10	–	–	3.9 (0.6)	5.0
11	–	–	4.4 (0.7)	6.6
12	–	–	5.1 (0.6)	3.1
13	–	–	5.5 (1.8)	3.9
14	–	–	5.9 (2.8)	4.1
15	–	–	6.0 (2.2)	6.6

TABLE VII. Parameters for the Lorentz oscillators given by Eq. (1) for the ordinary dielectric function $|\tilde{\varepsilon}_{11}|$ for NbAs. $\varepsilon^\infty = 1.4$ (Expt.) and 1.4 (DFT), $A_{\mathrm{UV}} = 1.4$ (Expt.) and 9.0 (DFT), $E_{\mathrm{UV}} = 6.7$ (Expt.) and 6.4 (DFT), $A_{\mathrm{IR}} = 12.2$ (Expt.). A DFT smearing factor of 0.02 eV was used.

Oscillators (n)	Expt. E_n (Γ_n) (eV)	Expt. A_n (a.u.)	DFT E_n (Γ_n) (eV)	DFT A_n (a.u.)
1	1.1 (0.2)	11.3	0.2 (0.3)	389.3
2	1.7 (2.4)	17.3	0.5 (0.3)	29.2
3	3.0 (0.9)	3.4	0.8 (0.4)	15.3
4	4.4 (1.5)	2.6	1.2 (0.4)	10.4
5	5.9 (5.6)	5.1	1.4 (0.6)	7.1
6	–	–	1.8 (0.5)	4.6
7	–	–	2.2 (1.5)	8.6
8	–	–	2.9 (0.4)	4.6
9	–	–	3.1 (0.3)	2.0
10	–	–	3.8 (0.5)	1.7
11	–	–	4.1 (0.4)	4.0
12	–	–	4.6 (0.6)	4.6
13	–	–	5.4 (0.3)	1.6
14	–	–	5.7 (1.3)	4.9

APPENDIX H: $\nabla_k(\Delta\varepsilon_{na})$ FOR TaAs AND NbAs

To better illustrate the VHS near the energies where SHG were measured, as discussed in Sec. III D and Appendix D, $\Delta\varepsilon_{na}$ and $\nabla_k(\Delta\varepsilon_{na})$ for selected pairs of bands presented in Figs. 4(b) and 7(b) are shown in Fig. 14. The VHSs are further confirmed by the dark arrows where $\nabla_k(\Delta\varepsilon_{na}) \approx 0$. Therefore, strong resonances near energies where large SHG were observed are enhanced by VHSs, and those VHSs are expected to enlarge the SHG response.

TABLE VI. Parameters for the Lorentz oscillators given by Eq. (1) for the ordinary dielectric function $|\tilde{\varepsilon}_{33}|$ for TaAs. $\varepsilon^\infty = 1.7$ (Expt.) and 1.9 (DFT), $A_{\mathrm{UV}} = 0.1$ (Expt.) and 49.8 (DFT), $E_{\mathrm{UV}} = 6.5$ (Expt.) and 6.9 (DFT), $A_{\mathrm{IR}} = 6.6$ (Expt.). A DFT smearing factor of 0.02 eV was used.

Oscillators (n)	Expt. E_n (Γ_n) (eV)	Expt. A_n (a.u.)	DFT E_n (Γ_n) (eV)	DFT A_n (a.u.)
1	1.2 (0.5)	8.0	0.3 (0.4)	12.4
2	1.8 (0.8)	4.6	0.4 (0.4)	14.9
3	2.2 (0.2)	1.6	0.8 (0.2)	2.4
4	2.8 (0.3)	0.8	1.1 (0.6)	15.6
5	3.0 (4.4)	12.4	1.7 (0.5)	8.3
6	4.1 (0.8)	2.8	2.0 (0.4)	6.5
7	6.2 (4.1)	5.0	2.4 (0.9)	13.5
8	–	–	2.8 (0.3)	2.9
9	–	–	3.0 (0.5)	6.1
10	–	–	3.2 (0.3)	2.3
11	–	–	3.5 (0.6)	5.4
12	–	–	4.0 (0.7)	10.5
13	–	–	4.5 (0.5)	4.3
14	–	–	5.1 (0.3)	0.7
15	–	–	5.6 (2.0)	13.3
16	–	–	5.7 (0.6)	0.9

TABLE VIII. Parameters for the Lorentz oscillators given by Eq. (1) for the ordinary dielectric function $|\tilde{\varepsilon}_{33}|$ for NbAs. $\varepsilon^\infty = 2.3$ (Expt.) and 2.0 (DFT), $A_{\mathrm{UV}} = 3.4$ (Expt.) and 48.4 (DFT), $E_{\mathrm{UV}} = 6.7$ (Expt.) and 6.8 (DFT), $A_{\mathrm{IR}} = 8.3$ (Expt.). A DFT smearing factor of 0.02 eV was used.

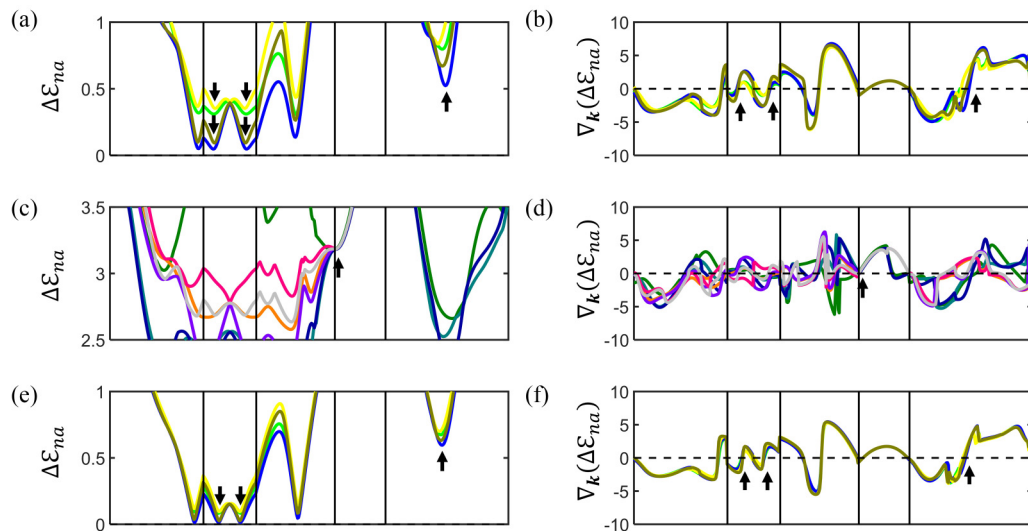| Oscillators (n)	Expt. E_n (Γ_n) (eV)	Expt. A_n (a.u.)	DFT E_n (Γ_n) (eV)	DFT A_n (a.u.)
1	1.5 (1.2)	20.1	0.1 (0.2)	66.6
2	1.9 (0.2)	1.9	0.6 (0.1)	3.5
3	2.6 (1.5)	10.2	0.8 (0.3)	10.8
4	3.5 (0.7)	3.0	1.1 (0.5)	12.8
5	4.6 (2.8)	4.7	1.5 (0.6)	11.7
6	5.5 (0.8)	3.5	1.8 (0.5)	11.6
7	6.4 (1.0)	2.9	2.1 (0.5)	8.9
8	–	–	2.4 (0.5)	10.5
9	–	–	2.8 (0.5)	7.7
10	–	–	3.2 (0.5)	7.9
11	–	–	3.6 (0.7)	6.9
12	–	–	4.1 (0.7)	7.1
13	–	–	4.6 (0.7)	4.9
14	–	–	5.1 (0.6)	5.2
15	–	–	5.4 (0.6)	9.7
16	–	–	6.0 (0.7)	10.5

FIG. 14. $\Delta\varepsilon_{na}$ and $\nabla_{\boldsymbol{k}}(\Delta\varepsilon_{na})$ of selected bands where Van Hove singularities (VHSs) are identified in TaAs and NbAs. Dark arrows indicate VHSs discussed in Sec. III D and Appendix D. (a) and (b) $\Delta\varepsilon_{na}$ and $\nabla_{\boldsymbol{k}}(\Delta\varepsilon_{na})$ of TaAs from 0 to 1 eV. (c) and (d) $\Delta\varepsilon_{na}$ and $\nabla_{\boldsymbol{k}}(\Delta\varepsilon_{na})$ of TaAs from 2.5 to 3.5 eV. (e) and (f) $\Delta\varepsilon_{na}$ and $\nabla_{\boldsymbol{k}}(\Delta\varepsilon_{na})$ of NbAs from 0 to 1 eV. The color codes are the same as presented in Figs. 4 and 7. Each legend shown at right corresponds to (a), (b); (c), (d); and (e), (f), respectively.

[1] H. Weyl, Elektron und gravitation. I, Z. Physik **56**, 330 (1929).

[2] S.-Y. Xu *et al.*, Discovery of a Weyl fermion semimetal and topological Fermi arcs, Science **349**, 613 (2015).

[3] S.-M. Huang, S.-Y. Xu, I. Belopolski, C.-C. Lee, G. Chang, B. Wang, N. Alidoust, G. Bian, M. Neupane, C. Zhang, S. Jia, A. Bansil, H. Lin, and M. Z. Hasan, A Weyl fermion semimetal with surface Fermi arcs in the transition metal monopnictide TaAs class, Nat. Commun. **6**, 7373 (2015).

[4] H. Weng, C. Fang, Z. Fang, B. A. Bernevig, and X. Dai, Weyl Semimetal Phase in Noncentrosymmetric Transition-Metal Monophosphides, Phys. Rev. X **5**, 011029 (2015).

[5] F. Arnold, C. Shekhar, S.-C. Wu, Y. Sun, R. D. dos Reis, N. Kumar, M. Naumann, M. O. Ajeesh, M. Schmidt, A. G. Grushin, J. H. Bardarson, M. Baenitz, D. Sokolov, H. Borrmann, M. Nicklas, C. Felser, E. Hassinger, and B. Yan, Negative magnetoresistance without well-defined chirality in the Weyl semimetal TaP, Nat. Commun. **7**, 11615 (2016).

[6] L. X. Yang, Z. K. Liu, Y. Sun, H. Peng, H. F. Yang, T. Zhang, B. Zhou, Y. Zhang, Y. F. Guo, M. Rahn, D. Prabhakaran, Z. Hussain, S.-K. Mo, C. Felser, B. Yan, and Y. L. Chen, Weyl semimetal phase in the non-centrosymmetric compound TaAs, Nat. Phys. **11**, 728 (2015).

[7] B. Q. Lv, H. M. Weng, B. B. Fu, X. P. Wang, H. Miao, J. Ma, P. Richard, X. C. Huang, L. X. Zhao, G. F. Chen, Z. Fang, X. Dai, T. Qian, and H. Ding, Experimental Discovery of Weyl Semimetal TaAs, Phys. Rev. X **5**, 031013 (2015).

[8] C. Shekhar, A. K. Nayak, Y. Sun, M. Schmidt, M. Nicklas, I. Leermakers, U. Zeitler, Y. Skourski, J. Wosnitza, Z. Liu, Y. Chen, W. Schnelle, H. Borrmann, Y. Grin, C. Felser, and B. Yan, Extremely large magnetoresistance and ultrahigh mobility in the topological Weyl semimetal candidate NbP, Nat. Phys. **11**, 645 (2015).

[9] I. Belopolski, S.-Y. Xu, D. S. Sanchez, G. Chang, C. Guo, M. Neupane, H. Zheng, C.-C. Lee, S.-M. Huang, G. Bian, N. Alidoust, T.-R. Chang, B. Wang, X. Zhang, A. Bansil, H.-T.

Jeng, H. Lin, S. Jia, and M. Z. Hasan, Criteria for Directly Detecting Topological Fermi Arcs in Weyl Semimetals, Phys. Rev. Lett. **116**, 066802 (2016).

[10] S.-Y. Xu *et al.*, Experimental discovery of a topological Weyl semimetal state in TaP, Sci. Adv. **1**, e1501092 (2015).

[11] J. Hu, S.-Y. Xu, N. Ni, and Z. Mao, Transport of topological semimetals, Annu. Rev. Mater. Res. **49**, 207 (2019).

[12] T. Liang, Q. Gibson, M. N. Ali, M. Liu, R. J. Cava, and N. P. Ong, Ultrahigh mobility and giant magnetoresistance in the Dirac semimetal Cd_3As_2, Nat. Mater. **14**, 280 (2015).

[13] X. Huang, L. Zhao, Y. Long, P. Wang, D. Chen, Z. Yang, H. Liang, M. Xue, H. Weng, Z. Fang, X. Dai, and G. Chen, Observation of the Chiral-Anomaly-Induced Negative Magnetoresistance in 3D Weyl Semimetal TaAs, Phys. Rev. X **5**, 031023 (2015).

[14] E. Liu *et al.*, Giant anomalous Hall effect in a ferromagnetic Kagomé-lattice semimetal, Nat. Phys. **14**, 1125 (2018).

[15] Q. Wang, Y. Xu, R. Lou, Z. Liu, M. Li, Y. Huang, D. Shen, H. Weng, S. Wang, and H. Lei, Author correction: large intrinsic anomalous Hall effect in half-metallic ferromagnet $Co_3Sn_2S_2$ with magnetic Weyl fermions, Nat. Commun. **9**, 4212 (2018).

[16] A. Sakai, Y. P. Mizuta, A. A. Nugroho, R. Sihombing, T. Koretsune, M.-T. Suzuki, N. Takemori, R. Ishii, D. Nishio-Hamane, R. Arita, P. Goswami, and S. Nakatsuji, Giant anomalous Nernst effect and quantum-critical scaling in a ferromagnetic semimetal, Nat. Phys. **14**, 1119 (2018).

[17] P. Li, J. Koo, W. Ning, J. Li, L. Miao, L. Min, Y. Zhu, Y. Wang, N. Alem, C.-X. Liu, Z. Mao, and B. Yan, Giant room temperature anomalous Hall effect and tunable topology in a ferromagnetic topological semimetal Co_2MnAl, Nat. Commun. **11**, 3476 (2020).

[18] Q. Ma, S.-Y. Xu, C.-K. Chan, C.-L. Zhang, G. Chang, Y. Lin, W. Xie, T. Palacios, H. Lin, S. Jia, P. A. Lee, P. Jarillo-Herrero, and N. Gedik, Direct optical detection of Weyl fermion chirality in a topological semimetal, Nat. Phys. **13**, 842 (2017).

[19] H. W. Liu, P. Richard, Z. D. Song, L. X. Zhao, Z. Fang, G.-F. Chen, and H. Ding, Raman study of lattice dynamics in the Weyl semimetal TaAs, Phys. Rev. B **92**, 064302 (2015).

[20] N. Sirica, R. I. Tobey, L. X. Zhao, G. F. Chen, B. Xu, R. Yang, B. Shen, D. A. Yarotski, P. Bowlan, S. A. Trugman, J.-X. Zhu, Y. M. Dai, A. K. Azad, N. Ni, X. G. Qiu, A. J. Taylor, and R. P. Prasankumar, Tracking Ultrafast Photocurrents in the Weyl Semimetal TaAs Using THz Emission Spectroscopy, Phys. Rev. Lett. **122**, 197401 (2019).

[21] B. Xu, Y. M. Dai, L. X. Zhao, K. Wang, R. Yang, W. Zhang, J. Y. Liu, H. Xiao, G. F. Chen, S. A. Trugman, J.-X. Zhu, A. J. Taylor, D. A. Yarotski, R. P. Prasankumar, and X. G. Qiu, Temperature-tunable Fano resonance induced by strong coupling between Weyl fermions and phonons in TaAs, Nat. Commun. **8**, 14933 (2017).

[22] B. Xu, Y. M. Dai, L. X. Zhao, K. Wang, R. Yang, W. Zhang, J. Y. Liu, H. Xiao, G. F. Chen, A. J. Taylor, D. A. Yarotski, R. P. Prasankumar, and X. G. Qiu, Optical spectroscopy of the Weyl semimetal TaAs, Phys. Rev. B **93**, 121110(R) (2016).

[23] S. Kimura, H. Yokoyama, H. Watanabe, J. Sichelschmidt, V. Süß, M. Schmidt, and C. Felser, Optical signature of Weyl electronic structures in tantalum pnictides Ta Pn ($Pn = P$, As), Phys. Rev. B **96**, 075119 (2017).

[24] D. Grassano, O. Pulci, A. Mosca Conte, and F. Bechstedt, Validity of Weyl fermion picture for transition metals monopnictides TaAs, TaP, NbAs, and NbP from *ab initio* studies, Sci. Rep. **8**, 3534 (2018).

[25] L. Wu, S. Patankar, T. Morimoto, N. L. Nair, E. Thewalt, A. Little, J. G. Analytis, J. E. Moore, and J. Orenstein, Giant anisotropic nonlinear optical response in transition metal monopnictide Weyl semimetals, Nat. Phys. **13**, 350 (2017).

[26] S. Patankar, L. Wu, B. Lu, M. Rai, J. D. Tran, T. Morimoto, D. E. Parker, A. G. Grushin, N. L. Nair, J. G. Analytis, J. E. Moore, J. Orenstein, and D. H. Torchinsky, Resonance-enhanced optical nonlinearity in the Weyl semimetal TaAs, Phys. Rev. B **98**, 165113 (2018).

[27] Z. Li, Y.-Q. Jin, T. Tohyama, T. Iitaka, J.-X. Zhang, and H. Su, Second harmonic generation in the Weyl semimetal TaAs from a quantum kinetic equation, Phys. Rev. B **97**, 085201 (2018).

[28] N. Nagaosa, T. Morimoto, and Y. Tokura, Transport, magnetic and optical properties of Weyl materials, Nat. Rev. Mater. **5**, 621 (2020).

[29] N. Sirica *et al.*, Photocurrent-driven transient symmetry breaking in the Weyl semimetal TaAs, arXiv:2005.10308.

[30] Y. Shao, Z. Sun, Y. Wang, C. Xu, R. Sankar, A. J. Breindel, C. Cao, M. M. Fogler, A. J. Millis, F. Chou, Z. Li, T. Timusk, M. B. Maple, and D. N. Basov, Optical signatures of Dirac nodal lines in NbAs$_2$, Proc. Natl. Acad. Sci. USA **116**, 1168 (2019).

[31] B. Q. Lv, N. Xu, H. M. Weng, J. Z. Ma, P. Richard, X. C. Huang, L. X. Zhao, G. F. Chen, C. E. Matt, F. Bisti, V. N. Strocov, J. Mesot, Z. Fang, X. Dai, T. Qian, M. Shi, and H. Ding, Observation of Weyl nodes in TaAs, Nat. Phys. **11**, 724 (2015).

[32] S. Furuseth, K. Selte, A. Kjekshus, S. Gronowitz, R. A. Hoffman, and A. Westerdahl, On the arsenides and antimonides of tantalum, Acta Chem. Scand. **19**, 95 (1965).

[33] S. Furuseth and A. Kjekshus, The crystal structure of NbAs (Comments), Acta Cryst. **17**, 1077 (1964).

[34] T. Besara, D. A. Rhodes, K.-W. Chen, S. Das, Q. R. Zhang, J. Sun, B. Zeng, Y. Xin, L. Balicas, R. E. Baumbach, E. Manousakis, D. J. Singh, and T. Siegrist, Coexistence of Weyl physics and planar defects in semimetals TaP and TaAs, Phys. Rev. B **93**, 245152 (2016).

[35] C.-L. Zhang, Z. Yuan, Q.-D. Jiang, B. Tong, C. Zhang, X. C. Xie, and S. Jia, Electron scattering in tantalum monoarsenide, Phys. Rev. B **95**, 085202 (2017).

[36] R. Sankar, G. Peramaiyan, I. P. Muthuselvam, S. Xu, M. Z. Hasan, and F. C. Chou, Crystal growth and transport properties of Weyl semimetal TaAs, J. Phys.: Condens. Matter **30**, 015803 (2017).

[37] N. J. Ghimire, Y. Luo, M. Neupane, D. J. Williams, E. D. Bauer, and F. Ronning, Magnetotransport of single crystalline NbAs, J. Phys.: Condens. Matter **27**, 152201 (2015).

[38] G. Kresse and J. Furthmüller, Efficient iterative schemes for ab initio total-energy calculations using a plane-wave basis set, Phys. Rev. B **54**, 11169 (1996).

[39] J. P. Perdew, K. Burke, and M. Ernzerhof, Generalized Gradient Approximation Made Simple, Phys. Rev. Lett. **77**, 3865 (1996).

[40] G. Kresse and D. Joubert, From ultrasoft pseudopotentials to the projector augmented-wave method, Phys. Rev. B **59**, 1758 (1999).

[41] H. Tompkins and E. A. Irene, *Handbook of Ellipsometry*, 1st edition (William Andrew, Inc., Norwich, 2006).

[42] M. Gajdoš, K. Hummer, G. Kresse, J. Furthmüller, and F. Bechstedt, Linear optical properties in the projector-augmented wave methodology, Phys. Rev. B **73**, 045112 (2006).

[43] S. N. Rashkeev, W. R. L. Lambrecht, and B. Segall, Efficient *ab initio* method for the calculation of frequency-dependent second-order optical response in semiconductors, Phys. Rev. B **57**, 3905 (1998).

[44] R. W. Boyd and D. Prato, *Nonlinear Optics*, 3rd edition (Academic Press, Amsterdam, Boston, 2008).

[45] S. A. Denev, T. T. A. Lummen, E. Barnes, A. Kumar, and V. Gopalan, Probing ferroelectrics using optical second harmonic generation, J. Am. Ceram. Soc. **94**, 2699 (2011).

[46] H. Padmanabhan, Y. Park, D. Puggioni, Y. Yuan, Y. Cao, L. Gasparov, Y. Shi, J. Chakhalian, J. M. Rondinelli, and V. Gopalan, Linear and nonlinear optical probe of the ferroelectric-like phase transition in a polar metal, LiOsO$_3$, Appl. Phys. Lett. **113**, 122906 (2018).

[47] A. J. Uzan, G. Orenstein, Á. Jiménez-Galán, C. McDonald, R. E. F. Silva, B. D. Bruner, N. D. Klimkin, V. Blanchet, T. Arusi-Parpar, M. Krüger, A. N. Rubtsov, O. Smirnova, M. Ivanov, B. Yan, T. Brabec, and N. Dudovich, Attosecond spectral singularities in solid-state high-harmonic generation, Nat. Photonics **14**, 183 (2020).

[48] A. H. Reshak, T. Ouahrani, R. Khenata, A. Otero-de-la-Roza, V. Luaña, and H. Baltache, Density functional calculation for the first and second harmonic generation of the chalcopyrite Ga$_2$AsSb, Comput. Mater. Sci. **50**, 886 (2011).

[49] L. Van Hove, The occurrence of singularities in the elastic frequency distribution of a crystal, Phys. Rev. **89**, 1189 (1953).

[50] J. Trull, R. Vilaseca, J. Martorell, and R. Corbalán, Second-Harmonic generation in local modes of a truncated periodic structure, Opt. Lett. **20**, 1746 (1995).

[51] M. Vandelli, M. I. Katsnelson, and E. A. Stepanov, Resonant optical second harmonic generation in graphene-based heterostructures, Phys. Rev. B **99**, 165432 (2019).

[52] C. J. Tabert and J. P. Carbotte, Optical conductivity of Weyl semimetals and signatures of the gapped semimetal phase transition, Phys. Rev. B **93**, 085442 (2016).

[53] M. Fox, *Optical Properties of Solids*, 2nd edition (Oxford University Press, Oxford, New York, 2010).

[54] Y. Luo, N. J. Ghimire, M. Wartenbe, H. Choi, M. Neupane, R. D. McDonald, E. D. Bauer, J. Zhu, J. D. Thompson, and F. Ronning, Electron-hole compensation effect between topologically trivial electrons and nontrivial holes in NbAs, Phys. Rev. B **92**, 205134 (2015).

[55] C. Zhang, Z. Ni, J. Zhang, X. Yuan, Y. Liu, Y. Zou, Z. Liao, Y. Du, A. Narayan, H. Zhang, T. Gu, X. Zhu, L. Pi, S. Sanvito, X. Han, J. Zou, Y. Shi, X. Wan, S. Y. Savrasov, and F. Xiu, Ultrahigh conductivity in Weyl semimetal NbAs nanobelts, Nat. Mater. **18**, 482 (2019).

[56] X. Yuan, C. Zhang, Y. Zhang, Z. Yan, T. Lyu, M. Zhang, Z. Li, C. Song, M. Zhao, P. Leng, M. Ozerov, X. Chen, N. Wang, Y. Shi, H. Yan, and F. Xiu, The discovery of dynamic chiral anomaly in a Weyl semimetal NbAs, Nat. Commun. **11**, 1259 (2020).

[57] F. Herman, C. D. Kuglin, K. F. Cuff, and R. L. Kortum, Relativistic Corrections to the Band Structure of Tetrahedrally Bonded Semiconductors, Phys. Rev. Lett. **11**, 541 (1963).

[58] R. G. Chambers, *Electrons in Metals and Semiconductors* (Springer, Netherlands, 1990).